Solid Earth

Discussions

Open Access

EGU

Unravelling the origins and P-T-t evolution of the allochthonous Sobrado unit (Órdenes Complex, NW Iberia) using combined U-Pb titanite, monazite and zircon geochronology and REE geochemistry

José Manuel Benítez-Pérez[1,3], Pedro Castiñeiras[2], Juan Gómez-Barreiro[3 (*)], José Ramón Martínez Catalán[3], Andrew Kylander-Clark[4], Robert Holdsworth[5]

[1]Centro de Ciências e Tecnologias Nucleares. Instituto Superior Técnico. Universidade de Lisboa. Estrada Nacional 10 (km 139,7), 2695-066, Bobadela LRS, Portugal
[2]Departamento de Mineralogía y Petrología. Facultad de Ciencias Geológicas, Universidad Complutense de Madrid. C/ José Antonio Novais, 12. Ciudad Universitaria, 28040, Madrid, Spain
[3]Departamento de Geología, Universidad de Salamanca, Pza. de los Caídos s/n, 37008, Salamanca, Spain
[4]Department of Earth Science, University of California, Santa Barbara, CA 93106, United States
[5]Earth Science Department, Durham University, Science Labs, Durham DH1 3LE, United Kingdom

Correspondence to: J. Gómez Barreiro (jugb@usal.es)

jose.benitez@ctn.tecnico.ulisboa.pt
castigar@geo.ucm.es
kylander@geol.ucsb.edu
r.e.holdsworth@durham.ac.uk

Abstract

The Sobrado unit, within the upper part of the Órdenes complex (NW Iberia) represents an allochthonous tectonic slice of exhumed high grade metamorphic rocks formed during a complex sequence of orogenic processes in the middle to lower crust. In order to constrain those processes, U-Pb geochronology and REE analyses of accessory minerals in migmatitic paragneisses (monazite, zircon), and mylonitic amphibolites (titanite) were conducted using LASS-ICP-MS. The youngest metamorphic zircon age obtained co-incides with a Middle Devonian concordia monazite age (~ 385 Ma) and is interpreted to represent the minimum age of the Sobrado high-P granulite-facies metamorphism that occurred during the early stages of the Variscan Orogeny. Metamorphic titanites from the mylonitic amphibolites yield a Late Devonian age (~ 365 Ma), and track the progressive exhumation of the Sobrado unit. In zircon, cathodoluminescence images and REE analyses allow two aliquots with different origins in the paragneiss to be distinguished. An Early Ordovician age (~ 490 Ma) was obtained for metamorphic zircons, employing the TuffZirc algorithm, although with a large analytical dispersion. This age is considered to mark the onset of granulite-facies metamorphism in the Sobrado unit under intermediate-P conditions, and related to intrusive magmatism and coeval burial in a magmatic arc setting. A maximum depositional age for the Sobrado unit is established in the late Cambrian (~ 503 Ma). The zircon dataset also record several inherited populations. The youngest cogenetic set of zircons yield a crystallization age from TuffZirc algorithm of ~ 530 Ma and are thought to be related to the peri-Gondwana magmatic arc. The additional presence of inherited zircons older than ~ 530 Ma is interpreted as suggesting a West African Craton provenance.

Keywords: U-Pb geochronology, LASS-ICP, zircon, titanite, monazite, REE, Sobrado Unit

1   **1.   Introduction**

2   Zircon, monazite and titanite are accessory mineral phases found in rocks with a very wide range
3   of compositions. These minerals can resist numerous sedimentary, igneous and metamorphic events
4   across a wide range of temperatures, pressures and strains, even when fluids are present. Frequently,
5   compositional domains can be defined in these minerals that record changes in different parameters (*e.g.*
6   Castiñeiras et al., 2010; Hacker et al., 2015; Stearns et al., 2016; Stipska et al., 2016; Storey et al., 2007;
7   Stübner et al., 2014). These minerals additionally provide several closed decay chains or disintegration
8   systems ($^{238}U \rightarrow \,^{206}Pb$, $^{235}U \rightarrow \,^{207}Pb$ y $^{232}Th \rightarrow \,^{208}Pb$), because they hold variable concentrations of
9   uranium (U) and/or thorium (Th) in their crystal lattices. Such variations in concentration allow accurate
10   dating using microscopic scale analysis (tens of microns size).

11   Titanite is stable in metabasites across a wide range of metamorphic conditions (Frost et al.,
12   2000; Spear, 1981) and is able to record metamorphic and deformational events (e.g. Franz and Spear,
13   1985; Rubatto and Hermann, 2001; Spencer et al., 2013; Stearns et al., 2016, 2015; Verts and Frost,
14   1996). The titanite U/Pb system is a widely used geochronometer for deformation events in granulite-
15   amphibolite facies rocks (*e.g.* Cherniak, 2006, Harlov et al., 2006, Spear, 1981). Monazite is common in
16   amphibolite facies and higher-grade facies Zoning in this mineral can have igneous or metamorphic
17   origins (DeWolf et al., 1993, Hawkins and Bowring, 1997, Spear and Pyle, 2002, Zhu et al., 1997). The
18   crystallization stages seen in zoned monazites, with changes in Y, Ca, Si, Sr, Ba, REE, U and Th can be
19   linked to certain metamorphic reactions (e.g. Corrie and Kohn, 2008; Kohn and Malloy, 2004) or
20   deformation process (*e.g.* Terry and Hamilton, 2000). Zircon survives the majority of magmatic,
21   metamorphic and erosive Earth processes. Catodoluminiscence analysis of zircon zoning patterns allows
22   a large variety of reactions to be distinguished and can clarify the petrologenetic evolution (Corfu et al.,
23   2003). Th/U ratios can also be used to separate zircons of igneous or metamorphic origins (Hokada and
24   Harley, 2004, Hoskin, 2005, Hoskin and Ireland, 2000, Möller et al., 2002). Rare-earth element (REE)
25   abundances can also be used as a qualitative petrological indicator. Heavy rare-earth elements (HREE)
26   are preferentially incorporated into zircon compared to light rare-earth elements (LREE). Hence, the
27   normalised HREE slope can be used to interpret whether a zircon crystallized or recrystallized when
28   garnet and xenotime (YPO_4) were present, because these minerals also preferentially assimilate HREE in
29   the lattice (*e.g.* Hermann and Rubatto, 2003; Hoskin and Ireland, 2000; Rubatto, 2002; Rubatto et al.,
30   2009).

31   The events recorded in individual grains can be radiometrically dated employing combined laser
32   ablation analyses and catodoluminiscence (CL) images in zircons (Corfu et al., 2003) and compositional
33   maps obtained using electron microprobe (EMP) in monazite (Goncalves et al., 2005; Williams et al.,
34   2007) to recognize different grown zones. The chemical analysis, especially REE, links the development
35   of growth zones to specific metamorphic or deformative events (e.g. Chen et al., 2010; Frost et al., 2000;
36   Gagnevin and Daly, 2010; Holder et al., 2015; Rubatto, 2002; Whitehouse and Platt, 2003; Zheng et al.,
37   2007). Simultaneous geochronology and REE data can also be a powerful tool in the interpretation of
38   ages - this is known as REE-assisted geochronology (Castiñeiras et al., 2010).

39   In the present study, monazite and zircon ages of paragneisses and titanite ages of amphibolites
40   taken from separate, but presently adjacent tectonic slices of the high-P/high-T of Sobrado unit are
41   compared and interpreted using REE-assisted geochronology. This sheds new light upon the possible
42   origin, ages and relationships between the regional foliation development and the partial melting
43   processes that have occurred in the Sobrado unit.

44

45   **2.   Geological background**

46   The Allochthonous complexes in NW Iberia are remnants of a huge nappe stack preserved as
47   klippen in the core of late Variscan synforms. . They consist of units mostly of peri-Gondwanan

Solid Earth
Discussions

Open Access

EGU

1 derivation, which can be classified in three groups based on their structural position in the tectonic pile
2 and origin: The Upper, Middle and Lower allochthons.

3   The Upper Allochthon is a piece of the northern margin of Gondwana detached and drifted away
4 during the Cambro-Ordovician opening of the Rheic Ocean. The Middle Allochthon is formed by
5 lithospheric pieces of oceanic affinity, or oceanic supracrustal sequences that formed part of the Rheic
6 oceanic realm, and are often referred to as the ophiolitic units. The Lower Allochthon derives from distal
7 parts of the Gondwanan continental margin.

8   The Allochthon units are separated from the Iberian Autothocton by a series of kilometer-scale
9 imbricated sheets, known as the Parautochthon (Ribeiro et al., 1990), or Schistose Domain in Galicia
10 (NW Spain), consisting of a set of Paleozoic metasedimentary and volcanic rocks. The Parautochthon has
11 stratigraphic and igneous affinities with the Iberian autochthon of the Central Iberian Zone, and no
12 ophiolites occur between them. For these reasons it is interpreted as a distal part of the Gondwanan
13 continental margin (Farias et al., 1987, Dias da Silva et al., 2014).

14   The allochthonous units are regarded as a stack of Varican thrust sheets with associed tectonic
15 fabrics and metamorphic events. Due to the "piggy-back" nature of the sequence, the structurally higher
16 units are thought to represent the furthest travelled paleogeographic domains. Recumbent folds, thrusts
17 and extensional detachments formed during the Variscan collision are found in all three allochthonous
18 units (Martínez Catalán et al., 1999; Gómez-Barreiro et al., 2007).

19   Intrusive rocks in the Upper allochthon have been dated between 520 and 490 Ma and are
20 associated with the development of a magmatic arc and extension of crust (Abati et al., 2007, 1999,
21 Castiñeiras et al., 2010, Fernández-Suárez et al., 2007, Ordóñez Casado, 1998, Peucat et al., 1990). High-
22 P/high-T metamorphism in these units has been dated approximately between 405-390 Ma (Fernández-
23 Suárez et al., 2007, Fernandez-Suarez et al., 2002, Ordóñez Casado et al., 2001, Santos Zalduegui et al.,
24 1996). Ages between 390 and 375 Ma have been found in ophiolitic rocks (Dallmeyer et al., 1997, 1991;
25 Peucat et al., 1990) and ages from 375 to 365 Ma have been related to continental subduction (Abati et
26 al., 2010; Zalduegui et al., 1995). Thrust wedge collapse, in the middle and lower allochthonous units, is
27 thought to have happened between 390 and 365 Ma, followed by a collision in the internal zones around
28 365-330 Ma, causing further folding and thrusts (Dallmeyer et al., 1997, Martínez Catalán et al., 2009).
29 Afterwards, there was another extensional collapse phase until 315 Ma, followed by a final phase of
30 shortening and folding up until approximately 305 Ma related to the regional oroclinal bending in Iberia
31 (Aerden, 2004, Álvarez-Valero et al., 2014, Martínez Catalán, 2011, 2012).

32   The Upper Allochthon is further subdivided into high-P/high-T and intermediate-P units (Gómez
33 Barreiro et al., 2007). The present study focuses on two of the high-P/high T upper units. The origin of
34 the high-P event recorded in these units is controversial, but might reflect the accretion of the units into
35 the continental part of northern Gondwana, during the Early-Middle Devonian (400-390 Ma; Ballèvre et
36 al., 2014).

37   The Sobrado antiform consists of three tectonic slices bounded by two extensional detachments
38 (Fig 1). The lower horse comprises highly serpentinized ultramafic rocks with interlayered metabasite
39 units. The metabasites include eclogites (Omp + Grt + Qtz + Rt ± Ky and Zo, mineral abbreviations
40 according to Kretz, 1983) and related clynopyroxene-garnet rocks without primary plagioclase (Na-Di +
41 Grt + Qtz + Rt ± Zo), as well as other types of rocks derived from the retrogression and mylonitzation of
42 the early high-P stages. The intermediate slice is made up of migmatitic felsic gneisses (mainly
43 paragneisses), with frequent inclusions of high-P granulites (Na-Di + Grt + Pl + Qtz + Rt ± Ky). Relicts
44 of igneous protoliths are not preserved either in the lower or intermediate slices. The upper slice,
45 however, contains migmatitic felsic gneisses and mafic layers derived from deformed and recrystallized
46 gabbros with locally preserve relict igneous textures, reaching high-P granulite facies conditions. The
47 progressive transformation from gabbros to high-P granulites (Na-Di + Grt + Pl + Qtz + Rt) has occurred

1 in a series of different stages with a metamorphic peak at 13-17 kbar and 660-770ºC (Arenas and
2 Martínez Catalán, 2002).

3   The metamorphic evolution described by most authors in the Sobrado Unit suggests that felsic
4 gneisses underwent differing degrees of partial melting after the metabasites reached their peak pressure.
5 Consequently, the felsic gneisses are thought to have developed a regional foliation under amphibolite
6 facies conditions, as did the amphibolic gneisses, "flaser" amphibolites and fine-grained amphibolites.
7 This metamorphic evolution is described by Arenas and Martínez Catalán (2002) as a clockwise P-T path,
8 with a metamorphic peak of, at least, 15 kbar and >800ºC, followed by a strongly isothermal and
9 decompressive trajectory. This trajectory is interpreted to result from gravitational collapse of an
10 overthickened orogenic wedge (Gómez-Barreiro et al., 2007, Ballèvre et al., 2014). Although some
11 regional structures, such as the Fornás detachment (*e.g.* Gómez-Barreiro et al., 2007, Álvarez-Valero et
12 al., 2014) or the Corredoiras detachment (Díaz García et al., 1999), have been related to this gravitational
13 readjustment, no study has dealt with the development of these fabrics in any detail. Overall, it is thought
14 that the extensional flow has generated a pervasive thinning of the orogenic pile and that the preserved
15 sequence of tectonic slices is strongly condensed.

16 **3.   Methodology**
17   **3.1. Selected samples**

18   Two samples (*JBP-71-15A* and *JBP-71-21*) were selected from two structurally separate but
19 currently adjacent parts the high-P/high-T Sobrado unit, within the Órdenes complex, for laser ablation
20 (LASS-Laser Ablation Split Stream) analyses, including U–Pb geochronology and REE determinations.
21 The sample locations are presented in Figure 1. Sample *JBP-71-21* is a mylonitic fine-grained
22 amphibolite, without any preserved igneous relicts. It is located at the base of the upper tectonic slice and
23 comprises Hbl + Pl + Grt ± Cpx + Bt + Rt ± Ttn ± Ilm. Sample *JBP-71-15A* is a granulite facies
24 migmatitic paragneiss from the underlying intermediate tectonic slice. It comprises Qtz + Pl + Grt + Kfs
25 + Ky + Bt + Ilm + Rt and shows microscopic scale textural evidence of partial melting.

26   **3.2. Sample preparation**

27   Sample preparation was carried out at the laboratories of the Universidad Complutense of
28 Madrid. The rocks were crushed, pulverized and sieved to achieve a 0.1-0.5 mm grain size. A heavy
29 minerals concentration is achieved using a Wilfley ™ table. Then the minerals are separated using
30 magnetic separation and heavy liquids (methylene iodide, CH_2I_2). Zircon (translucent, colourless or light
31 brown), monazite (yellow) and titanite (white) grains are selected by handpicking, according to their
32 external morphology viewed under a binocular microscope. Most of the zircon grains have either
33 irregular (metamorphic) or elongate dipyramidal prism (igneous) shapes, or are equigranular in habit with
34 abrasion signs (detrital), with scarce mineral inclusions. Titanite grains are generally rounded, with a
35 larger grain size compared to monazite grains, which present a more variable grain size distribution and
36 an irregular habit or are even broken. All zircon, monazite and titanite grains collected were arranged
37 separately in parallel rows, mounted on glass slide with a double-sided adhesive and set in epoxy resin.
38 After the resin was cured, the surface was eroded using a wet abrasive silicon carbide abrasive paper
39 (4000 grit) and polished with 0.3 μm aluminium oxide. The surface was then coated with gold, to avoid
40 charging problems under the scanning electron microscope (SEM). Prior to isotopic analysis,
41 cathodoluminescence images (CL) of zircon grains were taken on a JEOL JSM-820 SEM, and
42 compositional maps of monazite grains were created on a JEOL Superprobe JXA-8900M microprobe
43 (National Center for Electron Microscopy, Madrid). Secondary electron images (SE) were also taken to
44 determine the exact location of the spots, identify the internal structure, and presence of inclusions and
45 defects in zircon, monazite and titanite grains.

46   **3.3. Mineral description**

Solid Earth
Discussions
Open Access
EGU

1   Titanite secondary electrons images reveal an average grain size of 100 μm, with irregular
2   morphologies, homogeneous compositions and the presence of solid inclusions. This grain size permits
3   large spatial resolution analyses (50 μm) to be carried out. La, Th, Y, U and Nd compositional maps were
4   conducted in monazite grains, but we focus here on thorium compositional maps because these generally
5   show the best developed compositional zonation. Monazite grains have an average grain size of 60-70 μm
6   and irregular or rounded morphologies. Thorium zoning never exceeds 30% of the grain and was taken
7   into account to select the spots for isotopic analysis. Several spots were analyzed in monazite crystals
8   with the greatest compositional contrasts to determine if different compositional zones correspond to
9   different growth stages in the monazite grains.

10   Cathodoluminescence images are useful to relate the crystallization of parts of zircon crystals to
11   specific igneous, metamorphic or deformational events (Corfu et al., 2003, Nasdala et al., 2003, Zeck et
12   al., 2004). Zircon grains from the paragneises display a wide variety of external morphologies (Fig. 2),
13   from pyramidal {101} (grains numbers 76, 33, 129, 62), fragmentary (grain numbers 15, 53, 61, 28) or
14   sub-rounded, metamorphic (grain numbers 25, 67) crystals. The grains have length-to-width ratios
15   between 3:1 and 2:1, and are generally free of solid inclusions (Fig. 2). It is common to image a
16   homogeneous xenocristic core in zircon grains and even a less luminescent mantle in some grains (grain
17   numbers 6, 77, 31, 5, 40). The core aspect is mainly rounded, with irregular or angular shapes. In most of
18   the zircon grains, the internal parts of the grains display an oscillatory zoning (grain numbers 71, 33, 81,
19   35), with different thicknesses, although in some cases, this zoning is faint (grain numbers 26, 57). There
20   are several grains with sectorial zones (grain numbers 17, 26, 27, 56, 45) parallel to the zircon c-axis
21   (Watson and Yan Liang, 1995) and even one case of soccerball zoning (grain number 82). The zoning
22   usually appears to be partially truncated and surrounded by a discontinuous poorly luminescent rim (grain
23   numbers 76, 79, 20).

24   **3.4. Analytical techniques**

25   U-Th/Pb, REE and Hf analyses of zircon, titanite and monazite were carried out using the laser
26   ablation split stream (LASS) at the University of California at Santa Barbara (UCSB). The samples were
27   ablated using a Photon Machines 193 nm ArF excimer ultraviolet laser with a HelEx ablation cell coupled
28   to a Nu Instruments Plasma high-resolution multi-collector inductively coupled plasma mass
29   spectrometer (MC-ICP-MS) and either a Nu Instruments AttoM high-resolution single-collector ICP or
30   an Agilent 7700S quadrupole ICP-MS (Kylander-Clark et al., 2013). This installation allows the
31   simultaneous isotopic and compositional (REE) analysis to be carried out. The laser spot diameter was 20
32   μm for zircon, 7-10 μm for monazite (Košler et al., 2001) and 50 μm for titanite (Stearns et al., 2016),
33   resulting in pit depths between 6 μm for monazite and 30 μm for titanite. The laser has a fluence of ~1
34   J/cm^2, and was fired twice to remove common Pb from the sample surface and this material was allowed
35   to wash out for 15 s, prior to the material being ablated at 3 Hz for 20 s. On the ICP-MS, the masses
36   ^{204}Pb+Hg, ^{206}Pb, ^{207}Pb, and ^{208}Pb were measured using ion counters, and the masses ^{232}Th and ^{238}U were
37   measured using Faraday detectors.

38   The U-Th/Pb standardization for monazite was carried out using sample 44069 (Aleinikoff et al.,
39   2006) as the primary reference material (RM), whereas the Bananeira sample was employed as primary
40   RM for trace element corrections (Kylander-Clark et al., 2013; Palin et al., 2013). Additionally, FC-1
41   (Horstwood et al., 2003), Trebilcock (Tomascak et al., 1996) and Bananeira were also used as secondary
42   monazite RM, allowing ^{206}Pb/^{238}U ages to be within 2% of their accepted values. U-Pb proportions in
43   titanite were corrected using Bear Laken (Aleinikoff et al., 2007) and Y1710C5 (Spencer et al., 2013) as
44   RM. 91500 (Wieldenbeck et al., 1995) and GJI (Jackson et al., 2004) were used as RM for zircon, both
45   for isotopic composition and trace element calibrations. Radiogenic lead versus common lead
46   (^{207}Pb/^{206}Pb) measurements require up to 2% additional external error attributable either to variation count
47   statistics, or ablation signal stability (Hacker et al., 2015b, Spencer et al., 2013). These external errors
48   were incorporated into the data in the experiments.

1   The Iolite plug-in v. 2.5 (Paton et al., 2011) for the Wavemetrics Igor Pro software was used to
2 improve and reduce the analyses (Hacker et al., 2015). The isotopic ratios $^{238}U/^{206}Pb$ and $^{207}Pb/^{206}Pb$ for
3 each analysis were plotted on Tera-Wasserburg diagrams using Isoplot and Topsoil programs (Ludwig,
4 2012; Zeringue et al., 2014). All date uncertainties are reported at the 95% confidence interval, assuming
5 a Gaussian distribution of measurement errors. Zircon, titanite and monazite REE analyses were
6 normalized against the McDonough and Sun (1995) chondrite values.

7 **4.   Results**

8   **4.1. Titanite (amphibolite, intermediate tectonic slice)**

9   Fifty-one titanite analyses were projected onto a Tera-Wasserburg concordia plot (Tera and
10 Wasserburg, 1972) (Fig. 3a). After a preliminary evaluation, twelve analyses were rejected due to either
11 high common Pb or high discordance (>10%) and were considered no further (Table 1). The remaining
12 analyses define a Pb/U semi-total isochron between the common or initial Pb (^{207}Pb) and radiogenic Pb
13 (^{206}Pb) (Ludwig, 1998). The isochron confirms the chemical homogeneity of the data (Stearns et al.,
14 2016) and it intercepts the concordia at 364.8 $\pm$ 4.5 Ma (2σ). Titanite chondrite-normalized REE
15 analyses are detailed in Table 1 and are shown in Fig. 3b. Titanite REE patterns are convex upwards,
16 relatively flat, with slight LREE depletions versus HREE with respect to chondrite. They generally lack a
17 europium anomaly (Eu*), but some analyses show a non-distinctive positive or negative anomaly.
18 Recrystallized titanites, in the presence of amphibole, show a similar REE pattern to amphiboles (*e.g.*
19 Chambefort et al., 2013), with an umbrella shape, indicating a metamorphic origin (Lesnov, 2013;
20 Mulrooney and Rivers, 2005).

21   **4.2. Monazite (paragneiss, upper tectonic slice)**

22   For monazite U/Th-Pb geochronology we investigated the thorium zoning in monazite grains to
23 assess whether or not different groups of ages were present in a single grain (Stübner et al., 2014). As
24 shown in Figure 4, there are no significant age differences between spots or zones with different Th
25 chemical concentrations in a single grain. The analyzed REE patterns are also very similar, but both
26 profiles become noisy when HREE concentrations decrease. However, this could be due to uncertainties
27 in measurement (lower counts) and the interference effects of intermediate rare-earth oxides (MREE)
28 (Holder et al., 2015).

29   Data from seventy-six U/Th-Pb monazite analyses are shown in Table 2 and displayed using a
30 Tera-Wasserburg concordia plot (Fig. 5a). Four of these analyses, not related to chemical zoning, were
31 discarded due to common Pb loss and were considered no further. The remaining analyses form a single
32 population (mean square of weighted deviation; MSWD = 0.48) centered on a concordia age of 382.5 $\pm$
33 1.0 Ma (2σ). Monazite geochemistry is shown in Figure 5b. REE patterns analyzed show an LREE
34 enrichment, HREE depletion and negative Y anomalies with respect to chondrite with little variation
35 within or between samples. The profiles suggest simultaneous crystallization of monazite with garnet
36 (Holder et al., 2015, Mottram et al., 2014, Rubatto, 2002, Rubatto et al., 2006), which is stable at
37 paragneisses typical temperatures and pressures. Negative Eu anomalies indicate a preferential
38 incorporation of europium to feldspars, in particular to K-feldspar, during melt crystallization (Buick et
39 al., 2010; Rubatto et al., 2013). These characteristics are compatible with monazite recrystallization in a
40 single pulse (MSWD <1) in the presence of garnet, indicating a metamorphic origin.

41   **4.3. U-Pb zircon (paragneiss, upper tectonic slice)**

42   Eighty-three analyses were performed on eighty zircon grains from the Sobrado paragneiss
43 (Table 3). Five analyses were rejected for age calculation due to high contents of common Pb (grain
44 numbers 7, 29, 64, 69, 73) and two others were rejected due to analytical errors (grain numbers 8, 36).
45 The zircon analyses are shown on a Wetherill concordia plot, with a zoomed-in inset for $^{206}U/^{238}U$ ages
46 less than 600 Ma (Fig. 6). A Tera-Wasserburg concordia plot (Fig. 7a) and an age histogram, with a
47 probability density diagram (Fig. 7b), also were plotted for ages less than 600 Ma, because data from this

1 age range are likely due to inheritance (Fig. 7). It is also possible that there is some inheritance older than
2 600 Ma, but the register is discontinuous and it is difficult to distinguish between protolith ages and
3 inherited ages.

4   There is a general correlation between zircon grain texture in cathodoluminescence and ^{206}U
5 /^{238}U ages. Two groups are recognized (Fig. 7b). The first group range in age from 380 to ca. 500 Ma and
6 share sub-rounded or fragmentary grain morphologies. Sixteen spots were performed on rims or poorly
7 luminescent homogeneous cores (Fig. 2). These concordant analyses present moderate U (125-989 ppm)
8 and Th (2-358 ppm) concentrations, and Th/U ratios ranging from ~ 0.01 to 0.82. The second group range
9 from ca. 500 to ca. 600 Ma (n=19), exhibit assorted morphologies, from fragmentary to dipyramidal or
10 euhedral, and are frequently dominated by oscillatory zoning. Zircon grains in this aliquot show Th/U
11 ratios ranging from 0.15 to 0.99, with relatively high U (37-1215 ppm) and Th (18-931 ppm)
12 concentrations. The divergence between the two groups is most clearly seen in a U/Th versus ^{206}Pb/^{238}U
13 age plot (Fig. 8). The younger age group (380-500 Ma) defines a flat trend, excluding analyses number 11
14 and 26, while the second group exhits a very different steep distribution.

15 **4.4. REE zircon (paragneiss, upper tectonic slice)**

16   The chondrite-normalized REE patterns of the Sobrado zircons giving ages less than 600 Ma are
17 shown in Figure 9. In general, this group has variable REE patterns with higher ∑REE values compared
18 to older zircons. Low La contents (0.01-0.38 ppm) make it unlikely that metamictization of the analyzed
19 zircons has occurred (*e.g.* Belousova et al., 2002, Castiñeiras et al., 2010, Hoskin, 2005). All patterns
20 present Ce/Ce* positive anomalies (0.175-119 ppm) and these are usually more pronounced in the 500-
21 600 Ma zircons group. This anomalous Ce content is related to the oxidation state of the original magma.
22 As a consequence, zircon accepts Ce^{4+} versus Ce^{3+}, because the former ions replace Zr directly, without
23 the need for a coupled substitution (Hoskin and Schaltegger, 2003). Likewise, the patterns show a
24 negative europium anomaly (Eu/Eu*= 0.08-0.79), with higher values in the analyses that show higher
25 LREE contents. Plagioclase growth or crystallization controls the Eu anomaly, because it incorporates all
26 Eu^{2+} available in the system, although the Eu anomaly could also be conditioned by oxygen fugacity (*e.g.*
27 Schaltegger et al., 1999). In general, the 500-600 Ma zircons aliquot present a quite similar HREE
28 pattern, with a steady positive slope, characteristic of magmatic zircons (e.g. Grimes et al., 2015, Hanchar
29 and Westrenen, 2007, Hoskin and Schaltegger, 2003, Whitehouse and Platt, 2003). However, the 380-500
30 Ma zircons aliquot has a much greater variation in HREE patterns. Most of the population shows a
31 negative slope or flat HREE pattern (nº 15, 59, 76, 79, 47, 67, 75, 53, 70), typical of a metamorphic
32 zircon that grows with in the presence of garnet (*e.g.* Chen et al., 2010; Cheng et al., 2009; Peters et al.,
33 2013; Rubatto et al., 2009; Stipska et al., 2016). The remaining population (grains numbers 25, 20, 26,
34 71, 10, 17, 11) has a magmatic HREE signature.

35 **5. Discussion**
36 **5.1. Petrogenesis of the Sobrado zircons**

37   Petrogenetic information about the different zircon groups, defined according to their age, can be
38 ascertained using their REE contents and various elemental ratios, such as Yb/Gd, Th/U, Ce/Sm, U/Ce,
39 Th and Hf (*e.g.* Barth and Wooden, 2010; Castiñeiras et al., 2011). On the Yb/Gd versus Th/U plot (Fig.
40 10a), most analyses of the 380-500 Ma aliquot define a Th/U ratio ranging from 0.01 to 0.25. This is
41 significantly lower than the 500-600 Ma aliquot ratios (Th/U= 0.15-1.77). Yb/Gd ratios present a wide
42 dispersion in both zircon groups. According to Wooden et al., (2006), in magmatic zircon a Th/U ratio
43 reduction is usually combined with an increase in Yb/Gd ratios as zircon crystallization temperatures
44 decrease, indicating a fractional crystallization process. In this case, the homogeneity of 500-600 Ma data
45 suggests that these processes have not occurred in the magmatic evolution. Lower Yb/Gd ratios in 380-
46 500 Ma aliquot indicate the presence of garnet in the paragneisses. Ce/Sm ratios allow assessment of the
47 degree of oxidation of the zircon crystallization system. Ce/Sm ratios less than 2, in the 380-500 Ma
48 aliquot case, indicate the presence of fluids rich in oxygen and water, proving the metamorphic origin of

1   theses zircons (Fig. 10b). Nevertheless, high Ce/Sm values indicate an oxygen fugacity in the system or a
2   magma fractionation (Belousova et al., 2002, Castiñeiras et al., 2010). Additionally, in the bi-logarithmic
3   plot of the U/Ce ratio versus Th concentration, a 1:1 line can be used to separate magmatic from
4   metamorphic zircons (Fig. 10c) (Bacon et al., 2012). This is because metamorphic zircon has higher U
5   concentration compared to igneous zircon, whereas Ce is higher in magmatic zircon (*e.g.* Hoskin and
6   Schaltegger, 2003). Noticeably, the 500-600 Ma zircon population entirely fits within the magmatic field
7   whereas 380-500 Ma zircon aliquot, except three atypical analyses (grain numbers 10, 11, 26), shares a
8   metamorphic origin. On a Eu/Eu* versus Hf concentration plot, the Hf homogeneity, ranging from 70000
9   to 110000 ppm, in the 500-600 Ma group suggests that fractional crystallization of the magma that
10   formed those zircons did not occur (Fig. 10d). The Eu anomaly seen in the Sobrado zircons is interpreted
11   to be a consequence of coeval plagioclase growth and has no clear association with any age group.

12   In U/Th versus $^{206}Pb/^{238}U$ ages, Yb/Gd versus Th/U, Ce/Sm versus Yb/Gd, U/Ce versus Th
13   concentration plots and HREE patterns, there are always some discordant analyses (grain numbers 10, 11,
14   26) within the 380-500 Ma aliquot. These analyses are interpreted to correspond to zircon derived from a
15   partially modified igneous protolith. The U/Pb isotopic ratios were altered due to Pb-loss but this did not
16   affect the REE patterns. This modification in the protolith might be due to partial melting processes
17   operating in the Sobrado paragneisses (Benítez-Pérez, 2017), causing an opening of the U-Pb system.

18   Different element relationships, chondrite-normalized REE patterns and HREE abundances,
19   define a clear trend for each age group. The older dataset, corresponding to 500-600 Ma zircon aliquot,
20   display high Ce/Sm and low U/Ce contents, negative negative Eu anomalies and positive HREE slopes.
21   These zircons can be interpreted as having crystallized in an igneous rock when plagioclase was stable
22   (*e.g.* Rubatto, 2002). The 380-500 Ma zircon aliquot shows evidence of divergent REE patterns with
23   respect to the igneous zircon, a decrease of HREE abundances, with lower Ce/Sm contents, and higher
24   U/Ce abundances and similar Eu anomalies. These features agree with the new zircon growth observed in
25   CL images (Fig. 2) during granulite-facies metamorphism in the presence of garnet (*e.g.* Rubatto et al.,
26   2006; Stipska et al., 2016).

27   **5.2. Age interpretation**

28   The youngest zircon data recorded (380.3 ± 8.7 Ma) are coherent with the monazite concordia
29   age (382.5 ± 1.0 Ma) in the migmatitic paragneises of the upper tectonic slice. This Middle Devonian age
30   (~ 385 Ma) can be interpreted to represent the *minimum* age of the metamorphic event in Sobrado unit,
31   which reached high-P granulite facies (Fernández-Suárez et al., 2007; Ordóñez Casado et al., 2001). It is
32   suggested that the recrystallized monazite captures the onset of the exhumation process in the migmatitic
33   paragneisses (Holder et al., 2015). Titanite recrystallized, within the mylonitized amphibolites of the
34   intermediate tectonic slice, in the Late Devonian (~ 365 Ma) and could be related to the onset of
35   retrograde metamorphic conditions. This variation could be generated by the prolongation of the
36   exhumation process, reaching amphibolite facies. The Late Devonian age lies close to the Ar/Ar age (376
37   ± 2.0 Ma), proposed for uppermost units of the Órdenes complex (Dallmeyer et al., 1997).

38   The U-Pb zircon age for each group was estimated using the TuffZirc method, developed by
39   Ludwig and Mundil (2002), which calculates the median by choosing the largest set of concordant
40   analyses that are statistically coherent. The best estimate obtained for the youngest dataset (380-500 Ma)
41   is 489.58 (+ 12.15 - 6.76) Ma, obtained by pooling together only six of sixteen analyses (Fig. 11a). This
42   dataset shows a large analytical dispersion. Data affected by positive age biases were not used in the
43   TuffZirc calculation, with a pronounced slope. However, the 380-500 Ma zircon aliquot shows a clear
44   correlation between its cathodoluminescence texture and its geochemistry. The age recorded in the
45   migmatitic paragneisses is thought to correspond to a metamorphic event, dated in the Early Ordovician
46   (~ 490 Ma), and is in very good agreement with upper high-P/high-T dates of equivalent units carried out
47   during previous studies (Kuijper, 1979 Peucat et al., 1990; Fernández-Suárez et al., 2002, 2007). This age
48   also coincides on those obtained from intermediate pressure (intermediate-P) units, where large plutons

1   were emplaced and there is a lack of later high-P/high-T metamorphism during the Devonian. The
2   westernmost upper intermediate-P units of the Órdenes Complex underwent a granulite-facies
3   metamorphism dated between ca. 500 and 485 Ma, contemporaneous with the intrusion of massive
4   gabbros and granodiorites related to Cambrian magmatic arc activity (Abati et al. al., 1999, 2003, 2007,
5   1999, Andonaegui et al., 2002, 2012, 2016, Castiñeiras et al., 2002, 2010). The granulite-facies
6   metamorphism is associated with heating produced by the intrusions, accompanied by a quick burial,
7   almost coeval with igneous emplacement (Abati et al., 2003, Castiñeiras, 2005, Fernández-Suárez et al.,
8   2007).

9   Clearly, the metamorphic event recorded in zircon is pre-Variscan and is therefore independent
10   of the high-P/high-T granulite-facies metamorphism that occurred during the Early-Middle Devonian that
11   has been identified in the underlying upper units, such as in Sobrado with 660-770°C and 13-17 kbar
12   (Arenas and Martínez Catalán, 2002), or 750-853°C and 11.5-15.4 kbar (Benítez-Pérez, 2017). Thus, not
13   only was the pre-Variscan metamorphism followed by a decompression stage that was associated with
14   partial melting (Fernández-Suárez et al., 2002), but also, later Devonian metamorphism and
15   decompression during exhumation occurred, leading to partial melting in paragneisses and basic
16   granulites (Fernández-Suárez et al., 2007). The notable slope observed in the TuffZirc plot from 486.3 ±
17   12.0 Ma (Fig. 11a) probably is the result of these exhumation, burial and new exhumation processes
18   accompanied by partial melting. Hence, the fusion causes the U-Pb system to open in the zircon formed
19   prior to this date.

20   **5.3. Inherited zircon**

21   The maximum depositional age of the high-P/high-T Sobrado unit is 502.4 ± 12.3 Ma (late
22   Cambrian). It represents the youngest date obtained from a detrital zircon (YSG-youngest single grain
23   age; Dickinson and Gehrels, 2009), which preserves abrasion signs caused by erosion and sedimentation
24   (grain number 61, Fig. 2). The value is comparable to other maximum depositional ages obtained from
25   similar units in the NW Iberia allochthonous complexes, such as the intermediate-P Betanzos uppermost
26   unit ca. 480 Ma (Early Ordovician) by Fernández-Suárez et al. (2003), reinterpreted as ca. 510-530 Ma
27   (middle-late Cambrian) by Fuenlabrada et al., (2010), and the intermediate-P Cariño uppermost unit ca.
28   510 Ma (Albert et al., 2015).

29   The best estimate age obtained is 530.37 (+7.60, -7.46) Ma, using the TuffZirc algorithm on a
30   group of eighteen analyses ranging from ca. 500 to 600 Ma (Fig. 11b). This age is obtained by pooling
31   together fifteen cogenetic analyses, showing oscillatory zoning in the cathodoluminescence images and
32   displaying a great homogeneity in fractional crystallization indexes (Th/U and Hf). This inherited zircon
33   dataset, with a median age of ~ 530 Ma, reveals a widespread magmatic event in early-middle Cambrian.
34   Similar age magmatism (ca. 520-500 Ma) is also recognized in other well-characterized higher units of
35   the allochthonous complexes (Castiñeiras et al., 2010; Peucat et al., 1990; Santos Zalduegui et al., 2002),
36   and is related to a magmatic arc creation around the periphery of Gondwana (Abati et al., 2007, 1999).

37   U-Pb geochronology studies of detrital zircons and Sm-Nd whole rock analyses in intermediate-
38   P units of NW Iberia upper allochthons (Betanzos unit, Fuenlabrada et al., 2010; Cariño gneisses, Albert
39   et al., 2015) may give an indication of the provenance of inherited zircons in the Sobrado migmatitic
40   paragneisses (Fig. 12). Two Neoproterozoic populations dispersed between 600 and 850 Ma correspond
41   to a possible recycling of Cadomian and Pan-African zircons (*e.g.* Ennih and Liegeois, 2008, Linnemann
42   et al., 2014). A Mesoproterozoic fraction, between 1.0 and 1.4 Ga, is also found in the Parautochthonous
43   (Díez Fernández et al., 2012), basal allochthonous units (Díez Fernández et al., 2010) and, to a lesser
44   extent, in the intermediate-P units of NW Iberia (Albert et al., 2015). These inherited zircons, although
45   scarce (Fernández-Suárez et al., 2003), likely have their origin in rocks derived from Saharan, Arabian-
46   Nubian and West African cratons, and presumably transported during the Cadomian orogeny (Gutiérrez-
47   Alonso et al., 2003). Paleoproterozoic populations range from 1.8 to 2.2 Ga, clustered at 2.1 Ga
48   (Fernández-Suárez et al., 2003), whose origins likely involve materials generated or reworked during the

Eburnian orogeny (Egal et al., 2002; Ennih and Liegeois, 2008) from the West African craton (Peucat et al., 2005). Finally, the Archean population in the Sobrado paragneisses ranges from 2.5 to 2.8 Ga (*e.g.* Schofield et al., 2012), and is likely related to intrusive events in the Western Reguibat Shield, the northern part of the West African craton (Albert et al., 2015), with some reworking processes of juvenile rocks formed at ca. 3.0 Ga (Potrel et al., 1998).

6. Conclusions

This study provides new age constraints on the processes that have affected the Sobrado unit, part of the Órdenes Complex, and allows some correlation with events recognized in other parts of the allochthonous high-P/high-T complexes of NW Iberia. Titanite, monazite and zircon dating, together with REE analyses have been combined together in these rocks for the first time in order to carry out a geochronological investigation of the amphibolites and paragneisses.

According to the analyses, the youngest ages recorded by the metamorphic zircons are coherent with the concordia monazite age obtained from seventy-six analyses in the paragneisses. The Middle Devonian age (~ 385 Ma) represents the minimum age of the Sobrado metamorphic event under high-P granulite-facies conditions and represents the first stages of the Variscan orogeny in this part of Iberia. Dating of metamorphic titanite in the amphibolite yields a Late Devonian age (~ 365 Ma) and is associated with very homogeneous REE patterns suggesting the prolongation of the exhumation process in the Sobrado unit, reaching amphibolite-facies metamorphic conditions. In zircon, there is a strong relationship between their textures, as seen in cathodoluminescence images (CL), REE patterns and $^{206}Pb/^{238}U$ ages. Metamorphic zircon defines an Early Ordovician age (~ 490 Ma) although showing a large analytical dispersion. This date is linked to the first pre-Variscan granulite-facies metamorphism seen in in Sobrado unit under intermediate-P conditions, and it is interpreted to be related to the intrusion of basic and intermediate composition rocks, and coeval with burial in a magmatic arc context.

The maximum depositional age of the Sobrado unit is suggested to be late Cambrian based on the age of the youngest inherited zircon (~ 503 Ma). From the inherited zircon dataset, all cogenetic zircon, yield a crystallization age of ~ 530 Ma (early-middle Cambrian), pointing to the formation of a peri-Gondwana magmatic arc. The protoliths of inherited zircon older than ~ 530 Ma from Sobrado unit are found in other Iberian complexes and are thought to be related to sources in the West African craton.

Data availability

The data are not publicly accessible

Supplement

There is no supplement related to this article.

Author contributions

JMBP, PC, JGB and JRMC contributed equally to the field, experimental and elaboration of the manuscript. AKC contributes to U-Pb-REE acquisition and RH participated in the writing of the text and the geological interpretation.

Competing interests

The authors declare that they have no conflict of interest.

Acknowledgements

Solid Earth
Discussions
Open Access
EGU

5

6 References

7 Abati, J., Dunning, G.R., Arenas, R., Díaz García, F., González Cuadra, P., Martínez Catalán, J.R.,
8 Andonaegui, P., 1999. Early Ordovician orogenic event in Galicia (NW Spain): Evidence from U-Pb ages
9 in the uppermost unit of the Ordenes Complex. Earth and Planetary Science Letters 165, 213–228.
10 doi:10.1016/S0012-821X(98)00268-4

11 Abati, J., Arenas, R., Martinez Catalán, J.R., Díaz García, F., 2003. Anticlockwise P-T Path of Granulites
12 from the Monte Castelo Gabbro (Ordenes Complex, NW Spain). Journal of Petrology 44, 305–327.
13 doi:10.1093/petrology/44.2.305

14 Abati, J., Castiñeiras, P., Arenas, R., Fernández-Suárez, J., Barreiro, J.G., Wooden, J.L., 2007. Using
15 SHRIMP zircon dating to unravel tectonothermal events in arc environments. The early Palaeozoic arc of
16 NW Iberia revisited. Terra Nova 19, 432–439. doi:10.1111/j.1365-3121.2007.00768.x

17 Abati, J., Gerdes, A., Suárez, J.F., Arenas, R., Whitehouse, M.J., Fernández, R.D., 2010. Magmatism and
18 early-Variscan continental subduction in the northern Gondwana margin recorded in zircons from the
19 basal units of Galicia, NW Spain. Bulletin of the Geological Society of America 122, 219–235.
20 doi:10.1130/B26572.1

21 Aerden, D.G.A.M., 2004. Correlating deformation in Variscan NW-Iberia using porphyroblasts;
22 implications for the Ibero-Armorican Arc. Journal of Structural Geology 26, 177–196.
23 doi:10.1016/S0191-8141(03)00070-1

24 Albert, R., Arenas, R., Gerdes, A., Sánchez-Martínez, S., Fernández-Suárez, J., Fuenlabrada, J.M., 2015.
25 Provenance of the Variscan Upper Allochthon (Cabo Ortegal Complex , NW Iberian Massif). Gondwana
26 Research 28, 1434–1448. doi:10.1016/j.gr.2014.10.016

27 Aleinikoff, J.N., Schenck, W.S., Plank, M.O., Srogi, L.A., Fanning, C.M., Kamo, S.L., Bosbyshell, H.,
28 2006. Deciphering igneous and metamorphic events in high-grade rocks of the Wilmington complex,
29 Delaware: Morphology, cathodoluminescence and backscattered electron zoning, and SHRIMP U-Pb
30 geochronology of zircon and monazite. Bulletin of the Geological Society of America 118, 39–64.
31 doi:10.1130/B25659.1

32 Aleinikoff, J.N., Wintsch, R.P., Tollo, R.P., Unruh, D.M., Fanning, C.M., Schmitz, M.D., 2007. Ages and
33 origins of rocks of the Killingworth dome, south-central Connecticut: Implications for the tectonic
34 evolution of southern New England. American Journal of Science 307, 63–118. doi:10.2475/01.2007.04

35 Álvarez-Valero, A.M., Gómez-Barreiro, J., Alampi, A., Castineiras, P., Martinez Catalán, J.R., 2014.
36 Local isobaric heating above an extensional detachment in the middle crust of a Variscan allochthonous
37 terrane (Ordenes complex, NW Spain). Lithosphere 6, 409–418. doi:10.1130/L369.1

38 Andonaegui, P., Castiñeiras, P., González Cuadra, P., Arenas, R., Sánchez Martínez, S., Abati, J., Díaz
39 García, F., Martínez Catalán, J.R.., 2012. The Corredoiras orthogneiss (NW Iberian Massif):
40 Geochemistry and geochronology of the Paleozoic magmatic suite developed in a peri-Gondwanan arc.
41 Lithos 128–131, 84–99. doi:10.1016/j.lithos.2011.11.005

42 Andonaegui, P., González Del Tánago, J., Arenas, R., Abati, J., Martínez Catalán, J.R., Peinado, M., Díaz
43 García, F., 2002. Tectonic setting of the Monte Castelo gabbro (Ordenes Complex, northwestern Iberian
44 Massif): Evidence for an arc-related terrane in the hanging wall to the Variscan suture. Special Paper of
45 the Geological Society of America 364, 37–56. doi:10.1130/0-8137-2364-7.37

1   Andonaegui, P., Sánchez-Martínez, S., Castiñeiras, P., Abati, J., Arenas, R., 2016. Reconstructing
2   subduction polarity through the geochemistry of mafic rocks in a Cambrian magmatic arc along the
3   Gondwana margin (Órdenes Complex, NW Iberian Massif). International Journal of Earth Sciences 105,
4   713–725. doi:10.1007/s00531-015-1195-x

5   Arenas, R., Martínez Catalán, J.R., 2002. Prograde development of corona textures in metagabbros of the
6   Sobrado unit (Ordenes Complex, northwestern Iberian Massif). Geological Society of America Special
7   Pa, 73–88. doi:10.1130/0-8137-2364-7.73

8   Bacon, C.R., Vazquez, J.A., Wooden, J.L., 2012. Peninsular terrane basement ages recorded by Paleozoic
9   and Paleoproterozoic zircon in gabbro xenoliths and andesite from Redoubt volcano, Alaska. Bulletin of
10 the Geological Society of America 124, 24–34. doi:10.1130/B30439.1

11 Ballèvre, M., Martínez Catalán J.R., López-Carmona, A., Pitra, P., Abati, J., Díez Fernández, R.,
12 Ducassou, C., Arenas, R., Bosse, V., Castiñeiras, P., Fernández-Suárez, J., Gómez Barreiro, J., Paquette,
13 J-L., Peucat, J-J, Poujol, M., Ruffet, G. and Sánchez Martínez, S., 2014. Correlation of the nappe stack in
14 the Ibero-Armorican arc across the Bay of Biscay: a joint French–Spanish project. Geological Society,
15 London, Special Publications, 405, .doi: 10.1144/SP405.13

16 Barth, A.P., Wooden, J.L., 2010. Coupled elemental and isotopic analyses of polygenetic zircons from
17 granitic rocks by ion microprobe, with implications for melt evolution and the sources of granitic
18 magmas. Chemical Geology 277, 149–159. doi:10.1016/j.chemgeo.2010.07.017

19 Belousova, E.A., Griffin, W.L., O'Reilly, S.Y., Fisher, N.I., 2002. Igneous zircon: trace element
20 composition as an indicator of source rock type. Contributions to Mineralogy and Petrology 143, 602–
21 622. doi:10.1007/s00410-002-0364-7

22 Benítez-Pérez, J.M., 2017. Quantitative study of texture in tectonites by diffraction. Contribution to
23 seismic anisotropy and orogenic rheology. University of Salamanca (PhD. Thesis). Spain.

24 Buick, I.S., Clark, C., Rubatto, D., Hermann, J., Pandit, M., Hand, M., 2010. Constraints on the
25 Proterozoic evolution of the Aravalli-Delhi Orogenic belt (NW India) from monazite geochronology and
26 mineral trace element geochemistry. Lithos 120, 511–528. doi:10.1016/j.lithos.2010.09.011

27 Castiñeiras, P., Andonaegui, P., Arenas, R., Martinez Catalán, J.., 2002. Descripción y resultados
28 preliminares del plutón compuesto de San Xiao, Complejo de Cabo Ortegal (noroeste del Macizo
29 Ibérico). Geogaceta 32, 111–114.

30 Castiñeiras, P., 2005. Origen y evolución tectonotermal de las unidades de O Pino y Cariño (Complejos
31 Alóctonos de Galicia). Laboratorio Xeolóxico de Laxe, Serie Nova Terra, 28, A Coruña.

32 Castiñeiras, P., García, F.D., Gómez-Barreiro, J., 2010. REE-assisted U-Pb zircon age (SHRIMP) of an
33 anatectic granodiorite: Constraints on the evolution of the A Silva granodiorite, Iberian allochthonous
34 complexes. Lithos 116, 153–166. doi:10.1016/j.lithos.2010.01.013

35 Castiñeiras, P., Navidad, M., Casas, J.M., Liesa, M., Carreras, J., 2011. Petrogenesis of Ordovician
36 Magmatism in the Pyrenees (Albera and Canigó Massifs) Determined on the Basis of Zircon Minor and
37 Trace Element Composition. The Journal of Geology 119, 521–534. doi:10.1086/660889

38 Chen, R.X., Zheng, Y.F., Xie, L., 2010. Metamorphic growth and recrystallization of zircon: Distinction
39 by simultaneous in-situ analyses of trace elements, U-Th-Pb and Lu-Hf isotopes in zircons from eclogite-
40 facies rocks in the Sulu orogen. Lithos 114, 132–154. doi:10.1016/j.lithos.2009.08.006

41 Cheng, H., King, R.L., Nakamura, E., Vervoort, J.D., Zheng, Y.F., Ota, T., Wu, Y.B., Kobayashi, K.,
42 Zhou, Z.Y., 2009. Transitional time of oceanic to continental subduction in the Dabie orogen: Constraints
43 from U-Pb, Lu-Hf, Sm-Nd and Ar-Ar multichronometric dating. Lithos 110, 327–342.
44 doi:10.1016/j.lithos.2009.01.013

1 Cherniak, D.J., 2006. Zr diffusion in titanite. Contributions to Mineralogy and Petrology 152, 639–647.
2 doi:10.1007/s00410-006-0133-0

3 Corfu, F., Hanchar, J.M., Hoskin, P.W.O., Kinny, P.D., 2003. Atlas of Zircon Textures, in: Hanchar,
4 J.M., Hoskin, P.W.O. (Eds.), Zircon. Reviews in Mineralogy and Geochemistry. Mineralogical Society of
5 America, pp. 468–500.

6 Corrie, S.L., Kohn, M.J., 2008. Trace-element distributions in silicates during prograde metamorphic
7 reactions : implications for monazite formation 451–464. doi:10.1111/j.1525-1314.2008.00769.x

8 Dallmeyer, R.D., Martínez Catalán, J.R., Arenas, R., Gil Ibarguchi, J.I., Gutiérrez-Alonso, G., Farias, P.,
9 Bastida, F., Aller, J., 1997. Diachronous Variscan tectonothermal activity in the NW Iberian Massif:
10 Evidence from 40Ar/39Ar dating of regional fabrics. Tectonophysics 277, 307–337. doi:10.1016/S0040-
11 1951(97)00035-8

12 Dallmeyer, R.D., Ribeiro, A., Marques, F., 1991. Polyphase Variscan emplacement of exotic terranes
13 (Morais and Bragança Massifs) onto Iberian successions: Evidence from 40Ar/39Ar mineral ages. Lithos
14 27, 133–144. doi:10.1016/0024-4937(91)90025-G

15 DeWolf, C.P., Belshaw, N., O'Nions, R.K., 1993. A metamorphic history from micron-scale
16 207pb/206pb chronometry of Archean monazite. Earth and Planetary Science Letters 120, 207–220.

17 Dias da Silva, I., Valverde-Vaquero, P., González-Clavijo, E., Díez-Montes, A. y Martínez Catalán, J. R.
18 2014. Structural and stratigraphical significance of U–Pb ages from the Mora and Saldanha volcanic
19 complexes (NE Portugal, Iberian Variscides). In: Schulmann, K., Martínez Catalán, J. R., Lardeaux, J.
20 M., Janousek, V. & Oggiano, G. (eds) The Variscan Orogeny: Extent, Timescale, the Formation of the
21 European Crust. Geological Society, London, Special Publications, 405. First published online February
22 25, 2014, http://dx.doi.org/10.1144/SP405.3

23 Díaz García, F., Martínez Catalán, J.R., Arenas, R., González Cuadra, P., 1999. Structural and kinematic
24 analysis of the Corredoiras detachment: evidence for early Variscan synconvergent extension in the
25 Ordenes Complex, NW Spain. International Journal of Earth Sciences 88, 337–351.

26 Dickinson, W.R., Gehrels, G.E., 2009. Use of U-Pb ages of detrital zircons to infer maximum
27 depositional ages of strata: A test against a Colorado Plateau Mesozoic database. Earth and Planetary
28 Science Letters 288, 115–125. doi:10.1016/j.epsl.2009.09.013

29 Díez Fernández, R., Catalán, J.R.M., Gerdes, A., Abati, J., Arenas, R., Fernández-Suárez, J., 2010. U-Pb
30 ages of detrital zircons from the Basal allochthonous units of NW Iberia: Provenance and paleoposition
31 on the northern margin of Gondwana during the Neoproterozoic and Paleozoic. Gondwana Research 18,
32 385–399. doi:10.1016/j.gr.2009.12.006

33 Díez Fernández, R., Martínez Catalán, J.R., Arenas, R., Abati, J., Gerdes, A., Fernández-Suárez, J., 2012.
34 U–Pb detrital zircon analysis of the lower allochthon of NW Iberia: age constraints, provenance and links
35 with the Variscan mobile belt and Gondwanan cratons. Journal of the Geological Society 169, 655–665.
36 doi:10.1144/jgs2011-146

37 Egal, E., Thiéblemont, D., Lahondère, D., Guerrot, C., Costea, C.A., Iliescu, D., Delor, C., Goujou, J.C.,
38 Lafon, J.M., Tegyey, M., Diaby, S., Kolié, P., 2002. Late Eburnean granitization and tectonics along the
39 western and northwestern margin of the Archean K??n??ma-Man domain (Guinea, West African Craton).
40 Precambrian Research 117, 57–84. doi:10.1016/S0301-9268(02)00060-8

41 Ennih, N., Liegeois, J.-P., 2008. The boundaries of the West African craton, with special reference to the
42 basement of the Moroccan metacratonic Anti-Atlas belt. The Boundaries of the West African Craton 1–
43 17. doi:10.1144/SP297.1

44 Farias, P., Gallastegui, G. et al. 1987. Aportaciones al conocimiento de la litoestratigrafía y estructura de
45 Galicia Central. Memo´rias da Faculdade de Ciências, Universidade do Porto, 1, 411–431.

1 Fernández-Suárez, J., Arenas, R., Abiati, J., Martinez Catalán, J.R., Whitehouse, M., Jeffries, T., 2007.
2 U-Pb chronometry of polymetamorphic high-pressure granulites: An example from the allochthonous
3 terranes of the NW Iberian Variscan belt. Geological Society of America Memoir, 469–488.
4 doi:10.1130/2007.1200(24).

5 Fernández-Suárez, J., Corfu, F., Arenas, R., Marcos, A., Martínez Catalán, J.R., Díaz García, F., Abati, J.,
6 Fernández, F.J., 2002. U-Pb evidence for a polyorogenic evolution of the HP-HT units of the NW Iberian
7 Massif. Contributions to Mineralogy and Petrology 143, 236–253. doi:10.1007/s00410-001-0337-2

8 Fernández-Suárez, J., Garcia, F.D., Jeffries, T.E., Arenas, R., 2003. Constraints on the provenance of the
9 uppermost allochthonous terrane of the NW Iberian Massif: inferences from detrital zircon U-Pb ages.
10 Terra Nova 15, 138–144.

11 Franz, G., Spear, F.S., 1985. Aluminous Titanite (sphene) fremo the eclogite zone, south-central Tauern
12 window, Austria. Chemical Geology 50, 33–46.

13 Frost, B.R., Chamberlain, K.R., Schumacher, J.C., 2000. Sphene (titanite): phase relations and role as a
14 geochronometer. Chemical Geology 172, 131–148.

15 Fuenlabrada, J., Arenas, R., Sánchez-Martínez, S., Díaz García, F., Castiñeiras, P., 2010. A peri-
16 Gondwanan arc in NW Iberia I: Isotopic and geochemical constraints on the origin of the arc-A
17 sedimentary approach. Gondwana Research 17, 338–351. doi:10.1016/j.gr.2009.09.007

18 Gagnevin, D., Daly, J.S., 2010. Zircon texture and chemical composition as a guide to magmatic
19 processes and mixing in a granitic environment and coeval volcanic system. doi:10.1007/s00410-009-
20 0443-0

21 Gómez-Barreiro, J., Martínez Catalán, J.R., Arenas, R., Castiñeiras, P., Abati, J., Díaz García, F.,
22 Wijbrans, J.R., 2007. Tectonic evolution of the upper allochthon of the Órdenes complex (northwestern
23 Iberian Massif): Structural constraints to a polyorogenic peri-Gondwanan terrane. Geological Society of
24 America 423, 315–332. doi:10.1130/2007.2423(15).

25 Goncalves, P., Williams, M.L., Jercinovic, M.J., 2005. Electron-microprobe age mapping of monazite.
26 American Mineralogist 90, 578–585. doi:10.2138/am.2005.1399

27 Grimes, C.B., Wooden, J.L., Cheadle, M.J., John, B.E., 2015. "Fingerprinting" tectono-magmatic
28 provenance using trace elements in igneous zircon. Contributions to Mineralogy and Petrology 170, 1–26.
29 doi:10.1007/s00410-015-1199-3

30 Gutiérrez-Alonso, G., Fernández-Suárez, J., Jeffries, T.E., Jenner, G.A., Tubrett, M.N., Cox, R., Jackson,
31 S.E., 2003. Terrane accretion and dispersal in the northern Gondwana margin. An Early Paleozoic
32 analogue of a long-lived active margin. Tectonophysics 365, 221–232. doi:10.1016/S0040-
33 1951(03)00023-4

34 Hacker, B.R., Kylander-clark, A.R.C., Holder, R., Andersen, T.B., Peterman, E.M., Walsh, E.O.,
35 Munnikhuis, J.K., 2015. Monazite response to ultrahigh-pressure subduction from U – Pb dating by laser
36 ablation split stream. Chemical Geology 409, 28–41. doi:10.1016/j.chemgeo.2015.05.008

37 Hanchar, J.M., Westrenen, W. Van, 2007. Rare earth element behavior in zircon–melt systems. Elements
38 3, 37–42.

39 Harlov, D., Tropper, P., Seifert, W., Nijland, T., Förster, H.-J., 2006. Formation of Al-rich titanite
40 (CaTiSiO4 O – CaAlSiO 4 OH) reaction rims on ilmenite in metamorphic rocks as a function of f H2O
41 and f O2. Lithos 88, 72–84. doi:10.1016/j.lithos.2005.08.005

42 Hawkins, D.P., Bowring, S.A., 1997. U-Pb systematics of monazite and xenotime : case studies from the
43 Paleoproterozoic of the Grand Canyon, Arizona 87–103.

Solid Earth
Discussions

Open Access

EGU

1   Hermann, J., Rubatto, D., 2003. Relating zircon and monazite domains to garnet growth zones : Age and
2   duration of granulite facies metamorphism in the Val Malenco lower crust. Journal of Metamorphic 21,
3   Issue 9. doi:10.1046/j.1525-1314.2003.00484.x

4   Hokada, T., Harley, S.L., 2004. Zircon growth in UHT leucosome: constraints from zircon-garnet rare
5   earth elements (REE) relations in Napier Complex, East Antarctica. Journal of Mineralogical and
6   Petrological Sciences 99, 180–190. doi:10.2465/jmps.99.180

7   Holder, R.M., Hacker, B.R., Kylander-clark, A.R.C., Cottle, J.M., 2015. Monazite trace-element and
8   isotopic signatures of (ultra) high-pressure metamorphism : Examples from the Western Gneiss Region,
9   Norway. Chemical Geology 409, 99–111. doi:10.1016/j.chemgeo.2015.04.021

10   Horstwood, M.S.A., Foster, G.L., Parrish, R.R., Noble, S.R., Nowell, G.M., 2003. Common-Pb corrected
11   in situ U–Pb accessory mineral geochronology by LA-MC-ICP-MS. The Royal Society of Chemistry 18,
12   837–846. doi:10.1039/b304365g

13   Hoskin, P.W.O., 2005. Trace-element composition of hydrothermal zircon and the alteration of Hadean
14   zircon from the Jack Hills, Australia. Geochimica et Cosmochimica Acta 69, 637–648.
15   doi:10.1016/j.gca.2004.07.006

16   Hoskin, P.W.O., Ireland, T.R., 2000. Rare earth element chemistry of zircon and its use as a provenance
17   indicator. Geology 28, 627–630. doi:10.1130/0091-7613(2000)28<627:REECOZ>2.0.CO

18   Hoskin, P.W.O., Schaltegger, U., 2003. The Composition of Zircon and Igneous and Metamorphic
19   Petrogenesis, in: Hanchar, J.M., Hoskin, P.W.O. (Eds.), Zircon. Reviews in Mineralogy and
20   Geochemistry. Mineralogical Society of America, pp. 27–62.

21   Jackson, S.E., Pearson, N.J., Griffin, W.L., Belousova, E.A., 2004. The application of laser ablation-
22   inductively coupled plasma-mass spectrometry to in situ U-Pb zircon geochronology. Chemical Geology
23   211, 47–69. doi:10.1016/j.chemgeo.2004.06.017

24   Kohn, M.J., Malloy, M.A., 2004. Formation of monazite via prograde metamorphic reactions among
25   common silicates : Implications for age determinations. Geochimica et cosmochimica Acta 68, 101–113.
26   doi:10.1016/S0016-7037(03)00258-8

27   Košler, J., Tubrett, M.N., Sylvester, P.J., 2001. Application of laser ablation ICP-MS to U-Th-Pb dating
28   of monazite. Geostandards Newsletter-the Journal of Geostandards and Geoanalysis 25, 375–386.
29   doi:10.1111/j.1751-908X.2001.tb00612.x

30   Kretz, R., 1983. Symbols for rock-forming minerals. American Mineralogist 68, 277–279.
31   doi:10.1016/0016-7037(83)90220-X

32   Kuijper, R.P., 1979. U-Pb systematic and petrogenetic evolution of infracrustal rocks in the Paleozoic
33   basement of Western Galicia, NW Iberia. WO Laboratory of Isotope Geology, Amsterdam.

34   Kylander-Clark, A.R.C., Hacker, B.R., Cottle, J.M., 2013. Laser-ablation split-stream ICP
35   petrochronology. Chemical Geology 345, 99–112. doi:10.1016/j.chemgeo.2013.02.019

36   Lesnov, F.P., 2013. Consistent patterns of rare earth element distribution in accessory minerals from
37   rocks of mafic-ultramafic complexes. Central European Journal of Geosciences 5, 112–173.
38   doi:10.2478/s13533-012-0121-z

39   Linnemann, U., Gerdes, A., Hofmann, M., Marko, L., 2014. The Cadomian Orogen: Neoproterozoic to
40   Early Cambrian crustal growth and orogenic zoning along the periphery of the West African Craton-
41   Constraints from U-Pb zircon ages and Hf isotopes (Schwarzburg Antiform, Germany). Precambrian
42   Research 244, 236–278. doi:10.1016/j.precamres.2013.08.007

43   Ludwig, K.R., 1998. On the Treatment of Concordant Uranium-Lead Ages. Geochimica et
44   Cosmochimica Acta 62, 665–676. doi:10.1016/S0016-7037(98)00059-3

1   Ludwig, K.R., Mundil, R., 2002. Extracting reliable U–Pb ages and errors from complex populations of
2   zircons from Phanerozoic tuffs. Geochimica et Cosmochimica Acta 66, 463.

3   Ludwig, K.R., 2012. User's Manual for ISOPLOT version 3.75. A Geochronological Toolkit for
4   Microsoft Excel. Berkeley Geochronology Center.

5   Martínez Catalán, J.R., Arenas, R., Díaz García, F., Abati, J., 1999. Allochthonous Units in the Variscan
6   Belt of NW Iberia: Terranes and Accretionary History, in: Sinha, A.K. (Ed.), Basement Tectonics 13:
7   Proceedings of the Thirteenth International Conference on Basement Tectonics Held in Blacksburg,
8   Virginia, U.S.A., June 1997. Springer Netherlands, Dordrecht, pp. 65–84. doi:10.1007/978-94-011- 4800-
9   9_5

10   Martínez Catalán, J.R., Arenas, R., Abati, J., Sánchez Martínez, S., Díaz García, F., Fernández Suárez, J.,
11   González Cuadra, P., Castiñeiras, P., Gómez Barreiro, J., Díez Montes, A., González Clavijo, E., Rubio
12   Pascual, F.J., Andonaegui, P., Jeffries, T.E., Alcock, J.E., Díez Fernández, R., López Carmona, A., 2009.
13   A rootless suture and the loss of the roots of a mountain chain: The Variscan belt of NW Iberia. Comptes
14   Rendus Geoscience 341, 114–126. doi:10.1016/j.crte.2008.11.004

15   Martínez Catalán, J.R., 2011. Are the oroclines of the Variscan belt related to late Variscan strike-slip
16   tectonics? Terra Nova 23, 241–247. doi:10.1111/j.1365-3121.2011.01005.x

17   Martínez Catalán, J.R., 2012. The Central Iberian arc, an orocline centered in the Iberian Massif and some
18   implications for the Variscan belt. International Journal of Earth Sciences 101, 1299–1314.
19   doi:10.1007/s00531-011-0715-6

20   McDonough, W.F., Sun, S.S., 1995. The composition of the Earth. Chemical Geology 120, 223–253.
21   doi:10.1016/0009-2541(94)00140-4

22   Möller, A., O'Brien, P.J., Kennedy, A., Kröner, A., 2002. Polyphase zircon in ultrahigh-temperature
23   granulites (Rogaland, SW Norway): Constraints for Pb diffusion in zircon. Journal of Metamorphic
24   Geology 20, 727–740. doi:10.1046/j.1525-1314.2002.00400.x

25   Mottram, C.M., Warren, C.J., Regis, D., Roberts, N.M.W., Harris, N.B.W., Argles, T.W., Parrish, R.R.,
26   2014. Developing an inverted barrovian sequence; insights from monazite petrochronology. Earth and
27   Planetary Science Letters 403, 418–431. doi:10.1016/j.epsl.2014.07.006

28   Mulrooney, D., Rivers, T., 2005. Redistribution of the rare-earth elements among coexisting minerals in
29   metamafic rocks across the epidote-out isograd: An example from the St. Anthony Complex, northern
30   Newfoundland, Canada. Canadian Mineralogist 43, 263–294. doi:10.2113/gscanmin.43.1.263

31   Nasdala, L., Zhang, M., Kempe, U., Panczer, G., Gaft, M., Andrut, M., Plötze, M., 2003. Spectroscopic
32   methods applied to zircon, in: Hanchar, J.M., Hoskin, P.W.O. (Eds.), Zircon. Reviews in Mineralogy and
33   Geochemistry. Mineralogical Society of America, pp. 427–467.

34   Ordóñez Casado, B., 1998. Geochronological studies of the pre-Mesozoic basement of the Iberian
35   Massif : the Ossa Morena zone and the Allochthonous Complexes within the Central Iberian zone.
36   doi:10.3929/ethz-a-002017279

37   Ordóñez Casado, B., Gebauer, D., Schäfer, H.J., Ibarguchi, J.I.G., Peucat, J.J., 2001. A single Devonian
38   subduction event for the HP/HT metamorphism of the Cabo Ortegal complex within the Iberian Massif.
39   Tectonophysics 332, 359–385. doi:10.1016/S0040-1951(00)00210-9

40   Palin, R.M., Searle, M.P., Waters, D.J., Parrish, R.R., Roberts, N.M.W., Horstwood, M.S.A., Yeh, M.W.,
41   Chung, S.L., Anh, T.T., 2013. A geochronological and petrological study of anatectic paragneiss and
42   associated granite dykes from the Day Nui Con Voi metamorphic core complex, North Vietnam:
43   Constraints on the timing of metamorphism within the Red River shear zone. Journal of Metamorphic
44   Geology 31, 359–387. doi:10.1111/jmg.12025

1 Paton, C., Hellstrom, J., Paul, B., Woodhead, J., Hergt, J., 2011. Iolite: Freeware for the visualisation and
2 processing of mass spectrometric data. Journal of Analytical Atomic Spectrometry 26, 2508.
3 doi:10.1039/c1ja10172b

4 Peters, T.J., Ayers, J.C., Gao, S., Liu, X.M., 2013. The origin and response of zircon in eclogite to
5 metamorphism during the multi-stage evolution of the Huwan Shear Zone, China: Insights from Lu-Hf
6 and U-Pb isotopic and trace element geochemistry. Gondwana Research 23, 726–747.
7 doi:10.1016/j.gr.2012.05.008

8 Peucat, J.J., Bernardgriffiths, J., Ibarguchi, J.I.G., Dallmeyer, R.D., Menot, R.P., Cornichet, J., Deleon,
9 M.I.P., 1990. Geochemical and Geochronological Cross-Section of the Deep Variscan Crust - the Cabo-
10 Ortegal High-Pressure Nappe (Northwestern Spain). Tectonophysics 177, 263–292.

11 Peucat, J.J., Capdevila, R., Drareni, A., Mahdjoub, Y., Kahoui, M., 2005. The Eglab massif in the West
12 African Craton (Algeria), an original segment of the Eburnean orogenic belt: Petrology, geochemistry and
13 geochronology. Precambrian Research 136, 309–352. doi:10.1016/j.precamres.2004.12.002

14 Potrel, A., Peucat, J.J., Fanning, C.M., 1998. Archean crustal evolution of the West African Craton:
15 example of the Amsaga Area (Reguibat Rise). U-Pb and Sm-Nd evidence for crustal growth and
16 recycling. Precambrian Research 90, 107–117. doi:10.1016/S0301-9268(98)00044-8

17 Ribeiro, A., Pereira, E. & Dias, R. 1990. Central-Iberian Zone. Allochthonous Sequences. Structure in the
18 Northwest of the Iberian Peninsula. In: Dallmeyer, R. D. y Martínez García, E. (eds) Pre-Mesozoic
19 Geology of Iberia. Springer, Berlin, 220–236.

20 Rubatto, D., Hermann, J., 2001. Exhumation as fast as subduction ? Geology 29, 3–6.

21 Rubatto, D., 2002. Zircon trace element geochemistry : distribution coefficients and the link between U-
22 Pb ages and metamorphism Zircon trace element geochemistry : partitioning with garnet and the link
23 between U – Pb ages and metamorphism. Chemical Geology 184, 123–138.

24 Rubatto, D., Hermann, R.G., Buick, I.S., 2006. Temperature and Bulk Composition Control on the
25 Growth of Monazite and Zircon During Low-pressure Anatexis (Mount Stafford , Central Australia).
26 Journal of Petrology 47, 1973–1996. doi:10.1093/petrology/egl033

27 Rubatto, D., Hermann, J., Berger, A., Engi, M., 2009. Protracted fluid-induced melting during Barrovian
28 metamorphism in the Central Alps. Contributions to Mineralogy and Petrology 158, 703–722.
29 doi:10.1007/s00410-009-0406-5

30 Rubatto, D., Chakraborty, S., Dasgupta, S., 2013. Timescales of crustal melting in the Higher Himalayan
31 Crystallines (Sikkim, Eastern Himalaya) inferred from trace element-constrained monazite and zircon
32 chronology. Contributions to Mineralogy and Petrology 165, 349–372. doi:10.1007/s00410-012-0812-y

33 Santos Zalduegui, J.F., Schärer, U., Gil Ibarguchi, J.I., 1995. Isotope constraints on the age and origin of
34 magmatism and metamorphism in the Malpica-Tuy allochthon, Galicia, NW Spain. Chemical Geology
35 121, 91–103. doi:10.1016/0009-2541(94)00123-P

36 Santos Zalduegui, J.F., Schärer, U., Gil Ibarguchi, J.I., Girardeau, J., 1996. Origin and evolution of the
37 Paleozoic Cabo Ortegal ultramafic-mafic complex (NW Spain): U-Pb, Rb-Sr and Pb-Pb isotope data.
38 Chemical Geology 129, 281–304. doi:10.1016/0009-2541(95)00144-1

39 Santos Zalduegui, J.F., Scharer, U., Gil Ibarguchi, J.I., Girardeau, J., 2002. Genesis of Pyroxenite-rich
40 Peridotite at Cabo Ortegal (NW Spain): Geochemical and Pb-Sr-Nd Isotope Data. J. Petrol. 43, 17–43.
41 doi:10.1093/petrology/43.1.17

42 Schaltegger, U., Fanning, C.M., Günter, D., Maurin, J.C., Schulmann, K., Gebauer, D., 1999. Growth,
43 annealing and recrystallization of zircon and preservation of monazite in high-grade metamorphism:

conventional and in-situ U-Pb isotope, cathodoluminescence and microchemical evidence. Contributions to Mineralogy and Petrology 134, 186–201.

Schofield, D.I., Horstwood, M.S.A., Pitfield, P.E.J., Gillespie, M., Darbyshire, F., O'Connor, E.A., Abdouloye, T.B., 2012. U-Pb dating and Sm-Nd isotopic analysis of granitic rocks from the Tiris Complex: New constaints on key events in the evolution of the Reguibat Shield, Mauritania. Precambrian Research 204–205, 1–11. doi:10.1016/j.precamres.2011.12.008

Spear, F.S., 1981. An experimental study of hornblende stability and compositional variability in amphibolite. American Journal of Science. doi:10.2475/ajs.281.6.697

Spear, F.S., Pyle, J.M., 2002. Apatite , Monazite , and Xenotime in Metamorphic Rocks, in: Kohn, M.J., Rakovan, J., Hughes, J.M. (Eds.), Phosphates: Geochemical, Geobiological, and Materials Importance. Reviews in Mineralogy and Geochemistry. doi:10.2138/rmg.2002.48.7

Spencer, K.J., Hacker, B.R., Kylander-clark, A.R.C., Andersen, T.B., Cottle, J.M., Stearns, M.A., Poletti, J.E., Seward, G.G.E., 2013. Campaign-style titanite U – Pb dating by laser-ablation ICP : Implications for crustal fl ow , phase transformations and titanite closure. Chemical Geology 341, 84–101. doi:10.1016/j.chemgeo.2012.11.012

Stearns, M.A., Cottle, J.M., Hacker, B.R., Kylander-Clark, A.R.C., 2016. Extracting thermal histories from the near-rim zoning in titanite using coupled U-Pb and trace-element depth profiles by single-shot laser-ablation split stream (SS-LASS) ICP-MS. Chemical Geology 422, 13–24. doi:10.1016/j.chemgeo.2015.12.011

Stearns, M.A., Hacker, B.R., Ratschbacjer, L., Rutte, D., Kylander-clark, A.R.C., 2015. Titanite petrochronology of the Pamir gneiss domes: Implications for middle to deep crust exhumation and titanite closure to Pb and Zr diffusion. Tectonics 34, 784–802. doi:10.1002/2014TC003774.Received

Stipska, P., Powell, R., Hacker, B.R., Holder, R., 2016. Uncoupled U / Pb and REE response in zircon during the transformation of eclogite to mafic and intermediate granulite (Blansk y les , Bohemian Massif). Journal of Meta 34, 551–572. doi:10.1111/jmg.12193

Storey, C.D., Smith, M.P., Jeffries, T.E., 2007. In situ LA-ICP-MS U – Pb dating of metavolcanics of Norrbotten , Sweden : Records of extended geological histories in complex titanite grains. Chemical Geology 240, 163–181. doi:10.1016/j.chemgeo.2007.02.004

Stübner, K., Grujic, D., Parrish, R.R., Roberts, N.M.W., Kronz, A., Wooden, J., Ahmad, T., 2014. Lithos Monazite geochronology unravels the timing of crustal thickening in NW Himalaya. LITHOS 210–211, 111–128. doi:10.1016/j.lithos.2014.09.024

Tera, F., Wasserburg, G.J., 1972. U-Th-Pb systematics in three Apollo 14 basalts and the problem of initial Pb in lunar rocks. Earth and Planetary Science Letters 14, 281–304. doi:10.1016/0012-821X(72)90128-8

Terry, M.P., Hamilton, M.A., 2000. Monazite geochronology of UHP and HP metamorphism , deformation , and exhumation , Nordoyane ... doi:10.2138/am-2000-11-1208

Tomascak, P.B., Krogstad, E.J., Walker, R.J., 1996. U-Pb Monazite Geochronology of Granitic Rocks from Maine: Implications for Late Paleozoic Tectonics in the Northern Appalachians. The Journal of Geology 104, 185–195.

Verts, L.A., Frost, C.D., 1996. U-Pb sphene dating of metamorphism : the importance of sphene growth in the contact aureole of the Red Mountain pluton , Laramie Mountains , Wyoming. Contributions to Mineralogy and Petrology 125, 186–199.

1   Watson, E.B., Yan Liang, 1995. A simple model for sector zoning in slowly grown crystals: implications
2   for growth rate and lattice diffusion, with emphasis on accessory minerals in crustal rocks. American
3   Mineralogist 80, 1179–1187.

4   Whitehouse, M.J., Platt, Æ.J.P., 2003. Dating high-grade metamorphism - constraints from rare-earth
5   elements in zircon and garnet. Contributions to Mineralogy and Petrology 145, 61–74.
6   doi:10.1007/s00410-002-0432-z

7   Wieldenbeck, M., Allé, P., Corfú, F., Griffin, W.L., Meier, M., Oberli, F., Quadt, A. Von, Roddick, J.C.,
8   Spiegel, W., 1995. Three Natural Zircon Standards for U-Th-Pb, Lu-Hf, Trace Element and REE
9   Analyses. Geostandards Newsletter 19, 1–23. doi:10.1111/j.1751-908X.1995.tb00147.x

10 Williams, M.L., Jercinovic, M.J., Hetherington, C.J., 2007. Microprobe Monazite Geochronology:
11 Understanding Geologic Processes by Integrating Composition and Chronology. Annual Review of Earth
12 and Planetary Sciences 35, 137–175. doi:10.1146/annurev.earth.35.031306.140228

13 Wooden, J.L., Mazdab, F.K., Barth, A.P., Miller, C.F., Lowery, L.E., 2006. Temperatures (Ti) and
14 compositional characteristics of zircon: early observations using high mass resolution on the USGS-
15 Stanford SHRIMP-RG. Geochimica et Cosmochimica Acta 70, A707. doi:10.1016/j.gca.2006.06.1533

16 Zeck, H.P., Wingate, M.T.D., Pooley, G.D., Ugidos, J.M., 2004. A Sequence of Pan-African and
17 Hercynian Events Recorded in Zircons from an Orthogneiss from the Hercynian Belt of Western Central
18 Iberia —an Ion Microprobe U– Pb Study 45, 1613–1629. doi:10.1093/petrology/egh026

19 Zeringue, J., Bowring, J.~F., McLean, N.~M., Pastor, F., 2014. Building Interactive Visualizations for
20 Geochronological Data. AGU Fall Meeting Abstracts.

21 Zhu, X.K., O'Nions, R.K., Belshaw, N.S., Gibb, A.J., 1997. Significance of in situ SIMS chronometry of
22 zoned monazite from the Lewisian granulites , northwest Scotland. Chemical Geology 5, 35–53.

23

24

25

26

27

28

29

30

31

32

33

34

35

36

37

38

39

40

1

2

3

4

5

6

7

8

9

10

11

12

13

14
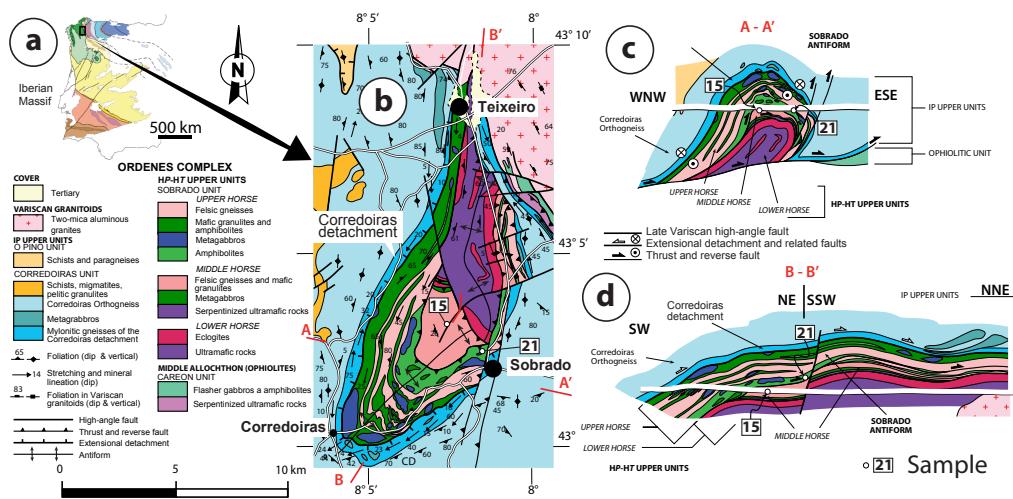
Figure 1. Geological map of the study area and location of the samples, modified from Arenas and Martínez Catalán (2002): (a) Location of the Órdenes complex within the Iberian massif. (b) Sobrado Unit map, indicating units and horses. (c) Cross-section in WNW-ESE direction and (d) SW-NE and SSW-NNE direction of the Sobrado antiform. Sample location are indicated.
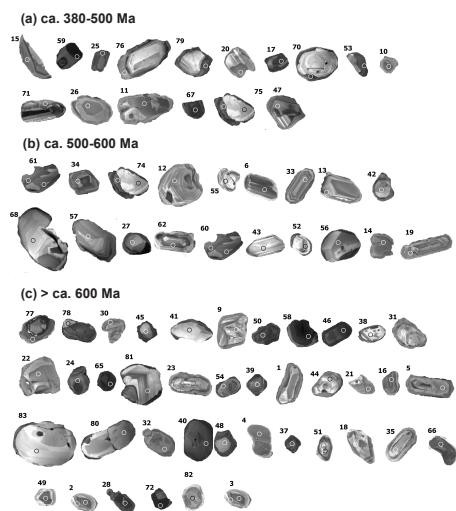
Figure 2. Cathodoluminescence (CL) images with analysed spots for all zircons. (a) ca. 380-500 Ma, first aliquot, (b) ca. 500-600 Ma, second aliquot, and (c) > ca. 600 Ma, third aliquot. The detailed results are in Table 3.
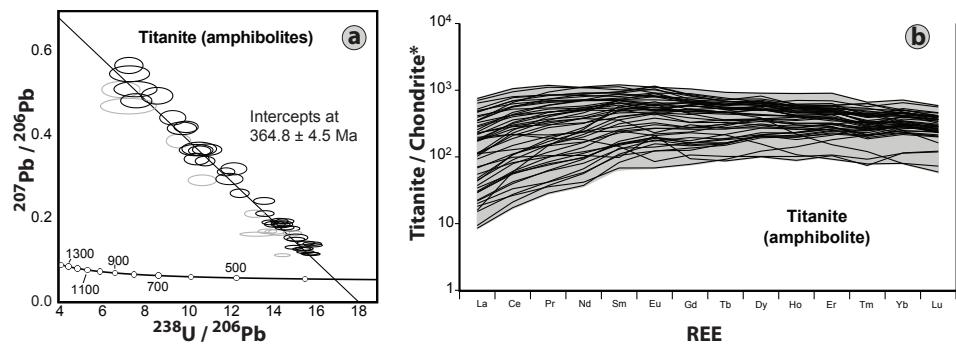
Figure 3. (a) Tera-Wasserburg diagram showing distribution of analysed titanites (n = 51) from Sobrado amphibolite (JBP-71-21). The rejected analyses are represented by gray ellipses. The ellipses represent the $^{207}Pb/^{206}Pb$ and $^{238}U/^{206}Pb$ errors (±2σ). (b) Chondrite-normalized rare earth element (REE) patterns for the same titanites.
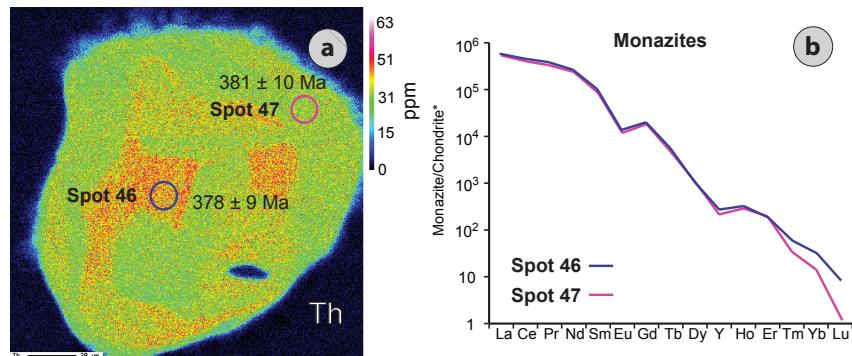
Figure 4. (a) Monazite grain compositional maps in paragneiss with a 30% thorium variation. Location and spot numbers (46 and 47) are indicated, as well as the [206]Pb/[238]U age and error (±2σ). (b) Chondrite-normalized rare earth element (REE) patterns for the same monazites in (a).
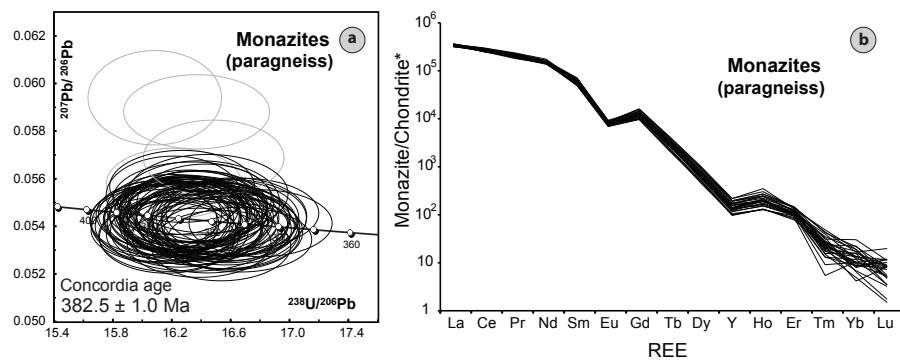
Figure 5. (a) Tera-Wasserburg diagram showing distribution of analysed monazites (n = 76) from Sobrado paragneiss (*JBP-71-15*). The rejected analyses are represented by gray ellipses. The ellipses represent the $^{207}Pb/^{206}Pb$ and $^{238}U/^{206}Pb$ errors (±2σ). (b) Chondrite-normalized rare earth element (REE) patterns for the same monazites.
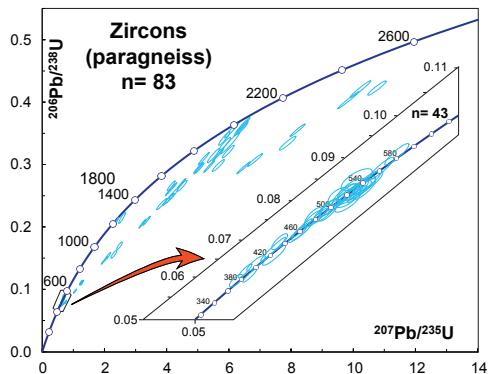
Figure 6. Wetherill concordia plot including all zircons (n= 83) in Sobrado paragneiss (*JBP-71-15)*. To better appreciate the young ages the most concordant dataset has been expanded (ca. 380 and 600 Ma; n = 43). The ellipses represent the $^{206}Pb/^{238}U$ and $^{207}Pb/^{235}U$ errors (±2σ).
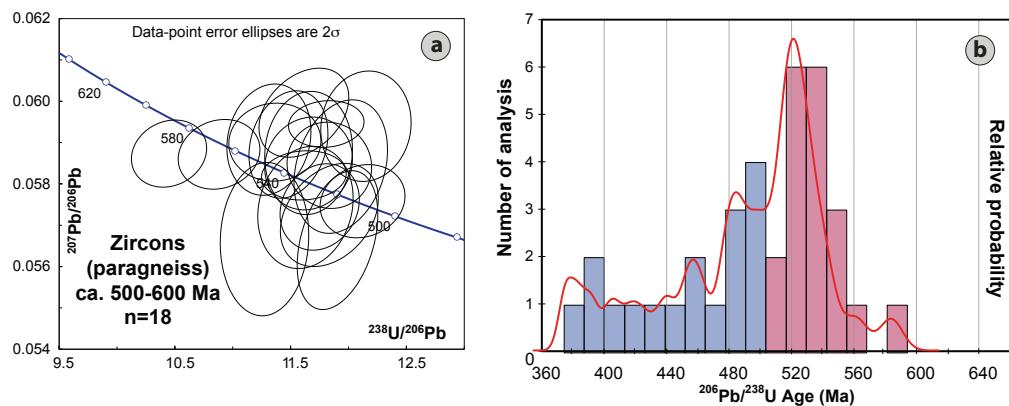
Figure 7. (a) Tera-Wasserburg diagram showing distribution of ca. 500-600 Ma zircon aliquot (n = 18) from Sobrado paragneiss (JBP-71-15). (b) Age histogram and probability density diagram (red line) for the same aliquot.
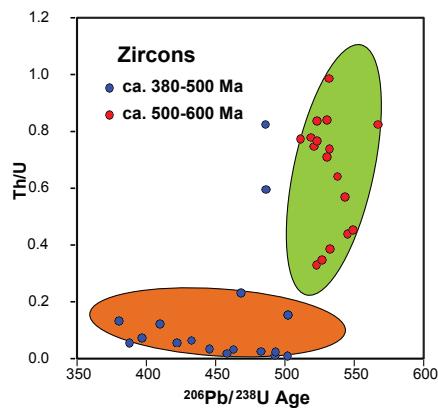
Figure 8. Th/U ratio versus $^{206}Pb/^{238}U$ ages plot for Sobrado zircons less than 600 Ma. Blue circles represent ca. 380-500 Ma population, whereas red circles represent ca. 500-600 Ma population.
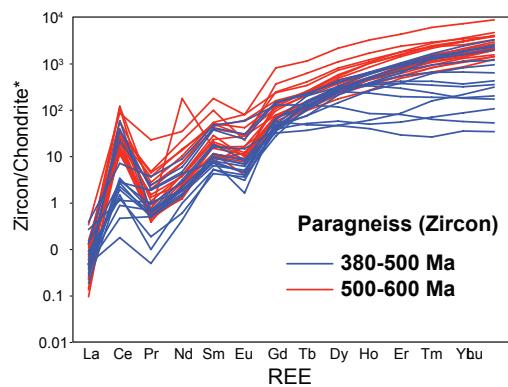
Figure 9. Chondrite-normalized rare earth element (REE) patterns for all zircon analyses less than 600 Ma. Blue lines are REE patterns of ca. 380-500 Ma zircon aliquot (n= 16) and red lines are REE patterns of ca. 500-600 Ma zircon aliquot (n= 19).
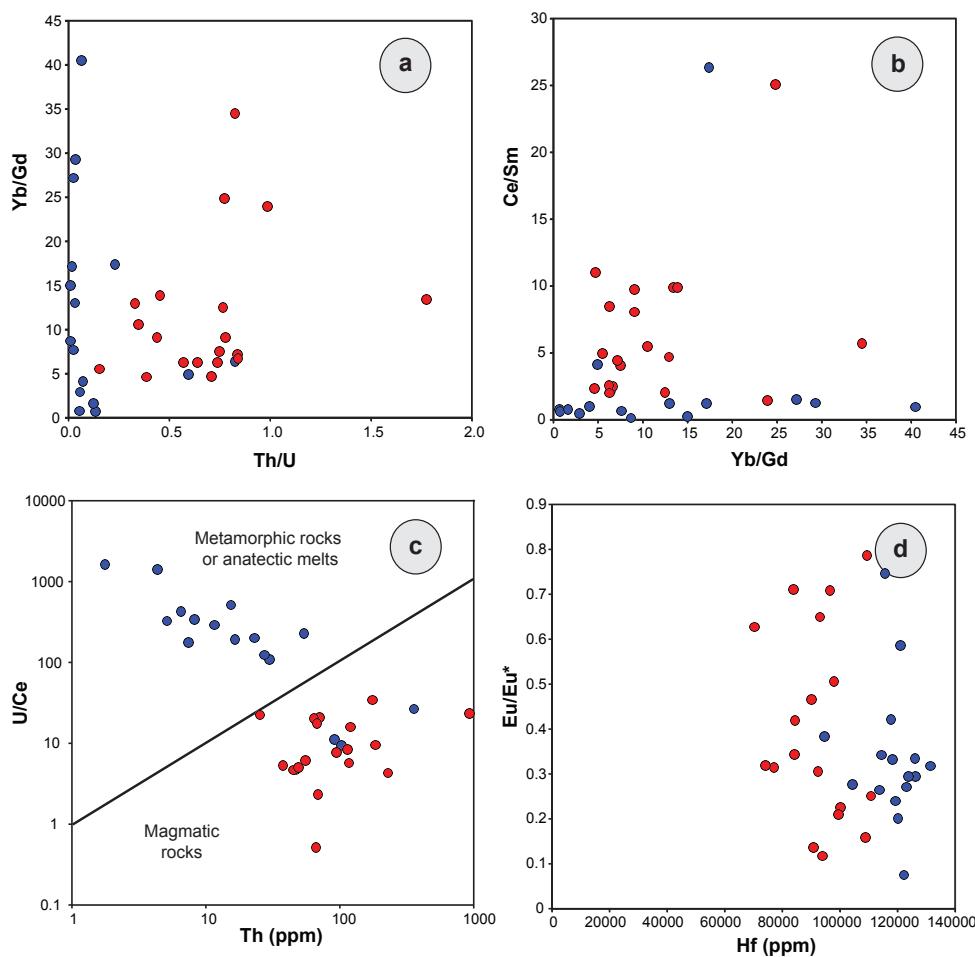
Figure 10. (a) Yb/Gd versus Th/U plot. (b) Ce/Sm versus Yb/Gd plot. (c) U/Ce versus Th (ppm) plot. (d) Eu/Eu* versus Hf (ppm) plot (Eu/Eu*=Eu/√(Sm*Gd)). Blue circles represent 380-500 Ma population and red circles represent 500-600 Ma population. See Section 5.1 for explanation.
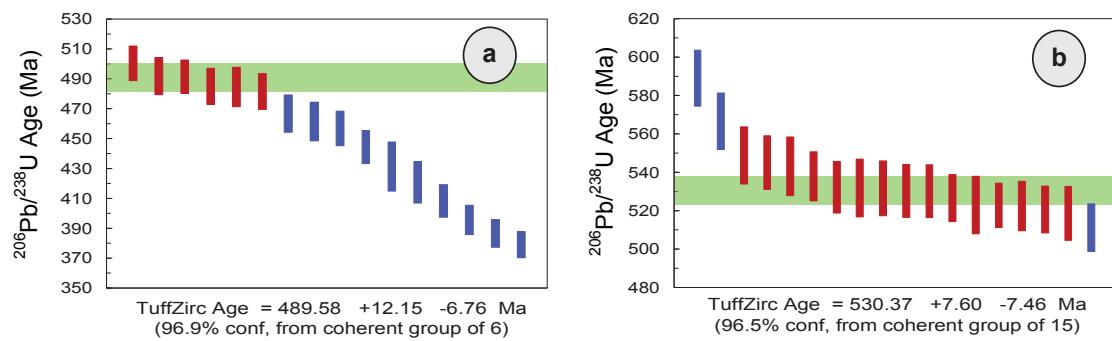
Figure 11. (a) Age distribution for 16 metamorphic zircons analysed, 380-500 Ma aliquot (b) Age distribution for 18 magmatic zircons analysed, 500-600 Ma aliquot. The blue bars are rejected analyses in the TuffZirc calculation, while the red bars are analyses used to obtain the best age estimate, and the green bar width reports the error (± 2σ). The box height is the estimated age with the error.
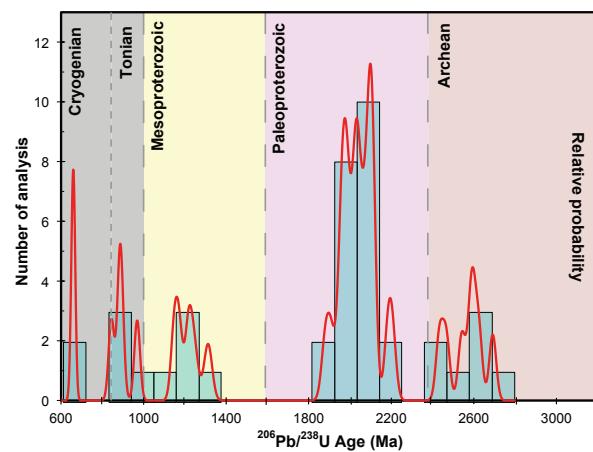
Figure 12. Age histogram and probability density diagram (red line) for ^{206}Pb/^{238}U ages older than 600 Ma for the Sobrado paragneiss (*JBP-71-15*). The different eras are indicated.

Table 1. U/Th–Pb analytical data and rare earth element (REE) for titanite (n= 51) from Sobrado amphibolite. 238U/206Pb, 207Pb/206Pb and 208Pb/232Th isotopic ratios are corrected for baselines, time-dependent laser-induced inter-element fractionation, plasma-induced fractionation, and instrument drift. Error corresponds to 2σ. Chondrite-normalized U, Th and REE (La, Ce, Pr, Nd, Sm, Eu, Gd, Tb, Dy, Ho, Er, Tm, Yb, Lu) abundances are expressed in ppm.

Spot	$^{238}U/^{206}Pb$	±	$^{207}Pb/^{206}Pb$	±	$^{208}Pb/^{232}Th$	±	U (ppm)	Th (ppm)	La (ppm)	Ce (ppm)	Pr (ppm)	Nd (ppm)	Sm (ppm)	Eu (ppm)	Gd (ppm)	Tb (ppm)	Dy (ppm)	Ho (ppm)	Er (ppm)	Tm (ppm)	Yb (ppm)	Lu (ppm)
1	15.59	0.35	0.1279	0.0032	0.02292	0.00053	7.42	16.57	751	1052	1182	1096	1012	1012	818	681	635	590	521	423.1	405	363.4
2	13.37	0.66	0.1625	0.0040	0.02580	0.00074	8.22	16.73	701	946	1107	1085	1128	904	889	762	661	584	483	333.6	324	232.9
3	13.74	0.36	0.2123	0.0056	0.03513	0.0101	4.16	7.44	327	424	520	538	650	588	574	559	522	538	532	411.7	465	392.7
4	13.85	0.36	0.1694	0.0045	0.05140	0.00298	4.30	2.47	116	188	275	318	484	519	503	471	419	408	365	278.9	299	230.5
5	13.70	0.41	0.2426	0.0067	0.05450	0.00376	2.71	2.35	109	209	297	383	511	561	458	437	422	416	386	287.9	315	261.4
6	14.20	0.40	0.1864	0.0058	0.03180	0.00119	3.16	4.74	225	300	369	409	547	671	515	539	495	526	511	393.5	448	383.7
7	12.06	0.52	0.2955	0.0111	0.15000	0.18002	2.00	1.46	68	111	153	199	314	382	329	361	373	394	399	318.6	340	290.7
8	14.52	0.33	0.1863	0.0050	0.03051	0.00091	4.86	7.93	394	574	681	705	762	813	685	648	589	608	579	436.8	504	417.1
9	15.11	0.35	0.1310	0.0037	0.02719	0.00074	6.55	10.39	471	692	733	803	861	828	714	679	703	703	693	565.6	650	561.0
10	12.55	0.37	0.2611	0.0083	0.14400	0.04010	2.35	0.96	45	90	152	217	359	442	328	329	300	291	304	252.6	290	245.5
11	15.48	0.35	0.1264	0.0034	0.03340	0.00137	8.13	6.22	350	654	938	1120	1201	1107	1045	928	902	890	901	659.9	711	586.6
12	7.30	1.08	0.4710	0.0153	0.07200	0.09601	0.61	0.32	15	27	42	67	134	140	162	189	214	233	264	248.2	287	232.1
13	10.02	0.47	0.4211	0.0111	0.11200	0.09503	1.20	0.69	31	61	98	139	244	209	230	214	156	108	93	78.5	80	72.8
14	9.66	0.47	0.3870	0.0135	0.22000	0.17006	1.09	0.56	29	55	79	96	159	197	160	181	200	213	249	230.4	296	242.7
15	13.99	0.32	0.1910	0.0046	0.03377	0.00107	4.58	6.10	184	317	421	512	599	485	518	467	433	401	374	319.8	306	236.2
16	14.41	0.41	0.1672	0.0063	0.03150	0.00144	4.02	5.44	216	359	421	492	642	501	609	609	590	549	545	471.3	464	395.9
17	14.94	0.36	0.1761	0.0048	0.13000	0.03609	4.38	0.71	43	108	170	239	404	460	433	485	572	540	536	488.3	420	339.0
18	7.35	0.77	0.5490	0.0155	-0.08000	-0.14001	0.55	0.30	18	26	36	42	68	68	77	92	122	141	181	210.9	230	204.5
19	15.96	0.36	0.1397	0.0034	0.02710	0.00071	8.10	9.22	414	520	541	580	692	609	652	624	708	579	591	630.8	507	405.7
20	15.04	0.36	0.1649	0.0049	0.03031	0.00096	6.39	8.79	293	426	468	522	543	499	482	455	514	419	438	446.6	412	321.1
21	11.90	0.34	0.3127	0.0079	0.37000	0.22012	2.91	0.40	48	108	185	276	507	426	527	465	385	218	153	120.2	80	59.3
22	14.41	0.34	0.1940	0.0054	0.05140	0.00216	5.29	3.73	255	465	598	716	889	794	766	709	603	458	595	629.1	472	382.1
23	14.18	0.37	0.1682	0.0046	0.09800	0.01612	4.77	1.43	102	228	355	458	710	718	687	604	671	488	476	449.4	344	258.5
24	15.92	0.35	0.1147	0.0030	0.02388	0.00057	10.78	13.20	468	695	829	915	901	1052	731	604	620	458	442	428.3	323	278.0
25	7.63	0.83	0.5120	0.0150	-0.03000	-0.49000	0.68	0.14	9	21	37	56	37	157	147	157	209	182	211	270.4	234	214.2
26	12.27	0.50	0.3200	0.0119	0.05770	0.00542	1.68	2.17	93	148	203	243	286	325	275	274	313	271	307	349.0	312	285.4
27	14.67	0.35	0.1937	0.0048	0.03279	0.00098	4.67	6.77	354	560	653	700	703	639	652	551	557	401	347	332.8	248	162.6
28	15.20	0.46	0.1543	0.0069	0.03350	0.00183	4.88	4.43	174	326	463	554	642	642	593	512	584	487	521	521.1	496	453.7
29	14.56	0.31	0.1120	0.0029	0.02158	0.00049	11.71	22.45	495	625	696	722	728	886	653	584	642	562	575	536.0	444	363.0
30	10.92	0.38	0.3387	0.0094	0.05840	0.00378	1.54	2.51	111	129	147	168	229	267	270	312	375	364	431	455.9	451	411.0
31	10.64	0.67	0.3680	0.0132	0.12200	0.03409	1.07	0.81	29	58	84	114	158	173	195	184	228	228	262	283.0	270	259.3
32	9.39	0.50	0.4430	0.0141	-0.02000	-0.12000	0.90	0.58	22	42	61	81	130	179	152	162	203	196	242	246.2	289	248.8
33	10.49	0.65	0.3651	0.0111	0.09500	0.00969	1.13	1.22	55	82	100	120	149	189	163	162	203	205	229	210.5	247	236.6
34	15.19	0.35	0.1501	0.0040	0.04200	0.00163	5.56	3.48	235	434	593	696	705	801	639	537	465	454	488	390.3	419	399.2
35	14.53	0.41	0.1866	0.0067	0.03390	0.00129	3.69	4.89	172	263	322	383	457	471	483	465	524	482	494	401.6	464	401.2
36	14.66	0.36	0.1785	0.0047	0.05840	0.00378	4.36	2.21	111	252	399	514	703	588	649	544	524	463	461	351.8	391	368.3
37	16.03	0.34	0.1359	0.0032	0.04720	0.00230	8.41	3.38	281	400	473	503	493	611	443	355	366	321	320	264.8	297	287.8
38	10.52	0.48	0.3435	0.0113	0.14400	0.06906	1.28	0.55	22	40	63	93	172	221	236	293	370	352	385	304.0	348	308.1
39	8.65	0.61	0.4960	0.0164	0.00000	0.00000	0.66	0.24	9	17	29	37	83	123	126	158	215	232	284	215.8	278	267.9
40	15.85	0.34	0.1160	0.0028	0.02681	0.00080	7.59	7.20	348	566	735	869	950	1151	862	731	739	619	632	420.2	530	460.6
41	11.89	0.31	0.1654	0.0046	0.06000	0.14001	2.54	0.09	16	60	148	259	580	512	585	518	425	425	428	291.9	411	362.2
42	9.82	0.57	0.4175	0.0124	0.13800	0.08205	0.95	0.79	71	99	105	105	98	210	94	87	100	89	104	74.5	115	122.0
43	15.67	0.34	0.1411	0.0037	0.02576	0.00068	6.21	10.38	640	799	852	832	803	913	671	607	625	520	493	319.8	397	362.2
44	11.01	0.57	0.3661	0.0111	0.11000	0.14002	1.20	0.86	34	57	75	99	154	196	174	218	270	274	316	272.5	369	345.9
45	7.67	0.60	0.4840	0.0139	0.04000	0.25000	0.57	0.33	20	33	42	58	105	123	136	150	193	200	221	204.0	263	280.5
46	13.25	0.39	0.2117	0.0071	0.03790	0.00242	2.61	4.41	228	284	304	324	395	455	384	348	358	302	284	195.5	227	204.9
47	10.78	0.54	0.2924	0.0105	0.13300	0.07405	1.66	0.79	37	79	118	165	255	304	277	309	340	313	321	253.8	305	288.2
48	6.94	0.74	0.5110	0.0158	0.07450	0.00570	0.64	1.89	173	290	339	376	356	230	303	269	273	260	255	186.6	217	199.2
49	15.64	0.33	0.1197	0.0028	0.03214	0.00100	10.32	7.50	521	772	845	886	937	1130	839	676	683	551	478	336.0	339	299.2
50	10.66	0.43	0.3635	0.0094	0.06970	0.00481	1.77	2.45	197	218	213	235	245	269	259	261	294	258	279	210.9	246	236.6
51	7.32	0.55	0.5690	0.0158	0.08940	0.08820	0.70	1.76	183	217	191	182	143	85	107	102	102	101	107	92.3	114	118.7

Solid Earth
Discussions
Open Access
EGU

Table 2. U/Th–Pb analytical data and rare earth element (REE) for monazite (n= 76) from Sobrado paragneiss. 238U/206Pb, 207Pb/206Pb and 208Pb/232Th isotopic ratios are corrected for baselines, time-dependent laser-induced inter-element fractionation, plasma-induced fractionation, and instrument drift. Error corresponds to 2σ. Chondrite-normalized U, Th and REE (La, Ce, Pr, Nd, Sm, Eu, Gd, Tb, Dy, Y, Ho, Er, Tm, Yb, Lu) abundances are expressed in ppm.

Spot	$^{238}U/^{206}Pb$		$^{207}Pb/^{206}Pb$		$^{208}Pb/^{232}Th$		U (ppm)	Th (ppm)	La (ppm)	Ce (ppm)	Pr (ppm)	Nd (ppm)	Sm (ppm)	Eu (ppm)	Gd (ppm)	Tb (ppm)	Dy (ppm)	Y (ppm)	Ho (ppm)	Er (ppm)	Tm (ppm)	Yb (ppm)	Lu (ppm)
1	16.29	±0.35	0.0543	±0.0013	0.01930	±0.00041	1640	26200	554430	433931	365302	243982	98243	12131	19989	4429	992	243	273	170	32.4	20	3.3
2	16.28	±0.35	0.0545	±0.0013	0.01916	±0.00042	1850	29300	527004	437194	352371	242451	94324	13286	19749	4490	1081	272	322	191	27.5	25	0.0
3	16.20	±0.38	0.0544	±0.0012	0.01949	±0.00044	1949	25500	519409	420881	346983	250109	107905	12451	23869	5319	1163	282	374	190	71.7	8	24.8
4	16.30	±0.38	0.0546	±0.0013	0.01930	±0.00047	1454	34200	563713	425775	323276	223632	85270	11474	18543	4266	898	192	251	118	46.6	6	12.2
5	16.18	±0.36	0.0543	±0.0012	0.01926	±0.00043	1805	32400	547257	420881	353448	231947	92568	11385	19899	4197	959	179	260	143	38.1	14	0.0
6	16.09	±0.35	0.0541	±0.0013	0.01946	±0.00044	1660	25900	524051	409462	338362	238074	96622	11794	19045	4634	980	227	291	184	44.5	19	5.7
7	16.27	±0.36	0.0544	±0.0012	0.01938	±0.00045	1790	29000	554430	442088	369612	230853	95676	12647	19598	4072	1045	248	310	172	46.6	20	30.5
8	16.15	±0.36	0.0545	±0.0012	0.01920	±0.00042	2170	44100	579325	437194	359914	248796	97838	13179	18693	3875	927	203	306	182	42.1	12	8.1
9	16.22	±0.37	0.0558	±0.0012	0.01900	±0.00043	2150	47100	567511	422512	340517	245295	90608	12451	17789	3958	902	232	286	179	52.2	6	25.6
10	16.38	±0.38	0.0549	±0.0012	0.01940	±0.00045	1680	27900	526160	435563	357759	242451	93919	12664	19799	4078	947	210	264	143	46.2	11	8.9
11	16.20	±0.37	0.0547	±0.0012	0.01930	±0.00044	1950	35700	555274	433931	383621	254923	95270	12060	19296	4432	996	221	321	181	44.1	17	5.7
12	16.29	±0.37	0.0546	±0.0012	0.01915	±0.00044	2280	32800	555274	415987	336207	252298	103176	12664	20201	4510	976	236	280	195	39.7	7	0.0
13	16.35	±0.36	0.0548	±0.0012	0.01897	±0.00044	2230	43200	540928	411093	349138	246827	94662	12202	18643	4551	976	221	282	138	16.2	13	0.0
14	16.28	±0.36	0.0545	±0.0012	0.01908	±0.00043	2060	41000	564135	438825	362069	230197	95608	12575	19296	4269	866	209	251	162	56.7	16	11.8
15	16.31	±0.39	0.0545	±0.0012	0.01920	±0.00044	2020	29600	535865	450245	378233	242888	109932	13268	22412	5125	1085	264	335	179	37.2	14	8.1
16	16.23	±0.36	0.0544	±0.0012	0.01953	±0.00044	1714	31400	562447	460033	391164	261050	103514	13748	19196	4432	988	211	244	182	25.5	10	12.2
17	16.40	±0.36	0.0546	±0.0012	0.01910	±0.00045	2360	37500	565401	429038	366379	241357	96689	12398	18884	4352	1004	218	291	177	48.2	17	8.9
18	16.22	±0.36	0.0545	±0.0012	0.01943	±0.00043	1662	30800	580591	464927	376078	262363	100000	12256	18884	4654	1081	228	308	168	34.0	4	3.3
19	16.25	±0.38	0.0538	±0.0012	0.01932	±0.00045	1600	31200	618143	442088	383621	244420	101419	12593	20050	4399	1024	217	253	161	30.8	18	2.8
20	16.11	±0.35	0.0543	±0.0012	0.01915	±0.00042	2190	34200	567932	427406	364224	240919	101351	12611	19899	4598	1012	238	300	201	39.7	17	6.9
21	16.17	±0.35	0.0543	±0.0012	0.01926	±0.00045	1804	28900	537975	443719	365302	243326	100608	13428	18693	4197	951	208	286	153	21.1	16	3.3
22	16.27	±0.35	0.0543	±0.0012	0.01964	±0.00044	2380	38200	560338	448613	383621	249672	101554	12913	19497	5125	1065	222	308	167	68.0	30	9.3
23	16.08	±0.37	0.0594	±0.0016	0.01886	±0.00044	1704	84000	562447	391517	327586	231947	87635	12487	16281	4019	951	246	264	215	31.2	19	40.7
24	16.18	±0.39	0.0536	±0.0012	0.01938	±0.00049	1650	29500	541772	417618	359914	238731	97230	12647	18693	4529	1110	246	315	188	79.4	12	11.0
25	16.37	±0.39	0.0546	±0.0012	0.01876	±0.00045	1900	57800	564557	417618	337284	232604	94797	11634	16935	4030	894	217	295	148	56.3	8	3.7
26	16.43	±0.39	0.0550	±0.0013	0.01922	±0.00044	1663	27800	566667	422512	360991	243545	97635	12700	17236	4488	963	249	288	184	47.8	17	14.6
27	16.32	±0.39	0.0549	±0.0012	0.01934	±0.00049	2000	32900	575949	432300	354526	249453	100608	13250	19347	4958	1167	255	306	177	45.7	25	7.3
28	16.35	±0.38	0.0538	±0.0011	0.01948	±0.00046	3680	28300	582700	445351	363147	243545	118243	15062	25025	6648	1553	383	443	213	43.3	16	16.7
29	16.58	±0.36	0.0539	±0.0012	0.01908	±0.00046	3050	32100	551899	432300	385776	240044	118243	14512	24171	6427	1451	352	399	221	30.4	24	7.7
30	16.27	±0.38	0.0546	±0.0012	0.01941	±0.00046	1822	27600	562447	440457	375000	260394	104054	13694	21156	5235	1102	240	332	191	51.8	18	16.7
31	16.63	±0.40	0.0544	±0.0013	0.01874	±0.00045	1926	28200	570042	437194	350216	232604	99324	11261	18693	4432	992	211	288	196	47.8	21	3.3
32	16.68	±0.42	0.0546	±0.0012	0.01915	±0.00047	2130	35500	542194	419250	371767	248359	102703	13144	18191	4834	996	243	291	168	39.3	8	0.0
33	16.36	±0.37	0.0541	±0.0012	0.01936	±0.00044	2220	29500	556540	414356	369612	257987	100338	13197	20402	4709	1053	248	300	174	21.9	16	13.4
34	16.42	±0.39	0.0544	±0.0012	0.01944	±0.00047	1950	30300	587342	407830	355603	255580	100000	12824	19648	4598	1041	253	289	166	64.4	16	18.3
35	16.39	±0.41	0.0542	±0.0012	0.01944	±0.00050	2480	32400	562025	412724	367457	245514	113446	14725	24372	6427	1439	341	452	231	49.4	3	24.8
36	16.31	±0.36	0.0544	±0.0012	0.01912	±0.00041	2010	43900	580591	402936	355603	258425	90405	10533	16935	4460	850	208	242	168	33.2	35	3.3
37	16.34	±0.44	0.0552	±0.0013	0.01948	±0.00050	2200	42200	582700	435563	365302	247046	100811	13002	21809	5512	1150	239	295	179	49.4	24	9.3
38	16.54	±0.38	0.0543	±0.0013	0.01913	±0.00046	2148	44200	571308	414356	363147	241794	92770	11829	18543	4645	1008	214	286	162	51.8	22	8.9
39	16.39	±0.44	0.0550	±0.0013	0.01960	±0.00053	1419	32800	568823	443719	365302	249234	91014	11901	16935	4598	907	222	287	157	45.3	17	6.1
40	16.44	±0.39	0.0542	±0.0012	0.01949	±0.00047	1930	31600	566540	424144	382543	257112	96757	12504	19598	4903	1175	256	326	203	41.3	28	20.7
41	16.37	±0.38	0.0548	±0.0012	0.01928	±0.00043	1690	40600	562447	435563	387931	262363	85405	11332	18342	4571	1045	239	333	178	27.9	12	13.4
42	16.56	±0.41	0.0544	±0.0013	0.01950	±0.00044	1655	34400	573418	420881	350216	243107	92095	12131	19246	4654	1037	231	321	164	21.5	16	0.0
43	16.26	±0.37	0.0545	±0.0013	0.01927	±0.00044	2490	37200	569198	432300	383621	245952	88108	10728	18291	4211	915	204	286	164	49.4	9	13.8
44	16.33	±0.40	0.0540	±0.0012	0.01942	±0.00047	2260	30300	585654	437194	376078	267396	95338	14369	19950	4737	1089	232	300	160	11.7	23	8.5
45	16.22	±0.37	0.0542	±0.0012	0.01942	±0.00045	1600	44700	528692	414356	329741	239168	87365	10906	18945	4820	1057	245	326	183	34.4	14	0.0
46	16.57	±0.41	0.0539	±0.0012	0.01907	±0.00049	1674	39800	538397	402936	328664	237199	85135	11812	18342	4681	1089	215	289	195	57.5	31	8.1
47	16.44	±0.42	0.0535	±0.0012	0.01927	±0.00048	1920	30300	528692	417618	351293	243326	94054	12771	18593	5208	1000	262	311	180	21.5	31	8.1
48	16.39	±0.40	0.0533	±0.0012	0.01936	±0.00049	1789	31400	540928	446982	350216	240263	89189	12220	17538	4349	898	202	317	151	24.7	19	5.7
49	16.21	±0.37	0.0553	±0.0013	0.01947	±0.00046	1810	35800	570464	430669	375000	262582	89459	12824	21859	5125	1264	283	308	190	24.7	8	2.4

Table 2. (cont.)

Spot	238U/206Pb	±	207Pb/206Pb	±	208Pb/232Th	±	U (ppm)	Th (ppm)	La (ppm)	Ce (ppm)	Pr (ppm)	Nd (ppm)	Sm (ppm)	Eu (ppm)	Gd (ppm)	Tb (ppm)	Dy (ppm)	Y (ppm)	Ho (ppm)	Er (ppm)	Tm (ppm)	Yb (ppm)	Lu (ppm)
50	16.40	0.37	0.0543	0.0012	0.01944	0.00045	2020	31600	561603	411093	340517	233479	92838	12131	19196	4598	1000	219	337	168	21.5	14	16.7
51	16.66	0.40	0.0534	0.0011	0.01944	0.00047	4730	33200	523207	432300	303879	243545	110135	14512	25879	6759	1650	358	575	217	79.8	31	7.7
52	16.54	0.40	0.0540	0.00122	0.01953	0.000469	1900	36500	585654	474715	359914	258425	111283.8	14547	21859	5983	1341	318	410	239	69.6	35.4	13.4
53	16.61	0.42	0.0544	0.00132	0.01891	0.000502	1596	66200	545992	412398	295259	233260	84932.43	11758	18593	4391	1085	255	308	212	30.0	11.2	5.3
54	16.49	0.39	0.0569	0.00129	0.01916	0.000475	1611	57800	542616	437194	352371	244201	100202.7	13499	20804	4931	1081	232	350	159	36.4	21.7	8.1
55	16.34	0.48	0.0537	0.00125	0.01950	0.000545	1760	30200	581013	476346	371767	246827	94729.73	13357	19899	4377	1024	193	251	169	32.8	25.5	5.7
56	16.80	0.40	0.0541	0.00115	0.01912	0.000446	2240	37600	536709	438825	335129	235449	84797.3	11758	16985	4177	996	204	288	164	40.9	28.6	8.1
57	16.49	0.41	0.0540	0.00113	0.01979	0.000522	3610	30800	526160	461664	355603	247484	111621.6	13979	26533	6648	1602	318	447	240	51.0	49.7	18.3
58	16.33	0.40	0.0544	0.00121	0.01965	0.000471	2110	39100	568354	464927	329741	240700	80000	11279	16030	3767	748	165	216	128	38.9	16.8	0.0
59	16.59	0.38	0.0542	0.0012	0.01946	0.000442	3130	33400	556118	461664	344828	250985	93648.65	11883	19698	4873	976	222	271	173	42.9	13.0	19.5
60	16.59	0.38	0.0540	0.0012	0.01944	0.000447	3270	30600	567511	450245	322198	245733	111283.8	13854	23819	5956	1524	323	445	236	36.4	16.8	19.5
61	16.55	0.42	0.0537	0.00124	0.01905	0.00045	1860	69500	540928	433931	309287	224508	87702.7	12256	16683	3518	752	174	209	156	36.4	6.8	13.4
62	16.14	0.40	0.0538	0.00114	0.01945	0.000517	3700	34000	579325	481240	346983	233260	114189.2	14760	25226	6288	1467	359	498	232	72.1	27.3	32.5
63	16.35	0.38	0.0539	0.00121	0.01971	0.000462	2030	32300	582700	477977	342672	245733	94256.76	13464	18894	4343	967	227	255	166	38.9	36.6	8.9
64	16.45	0.44	0.0554	0.00135	0.01954	0.000525	1700	32600	584388	461664	345905	228665	100000	12398	22010	5457	1248	287	397	194	44.9	22.4	14.2
65	16.59	0.40	0.0538	0.00132	0.01921	0.00047	1476	33600	602532	453507	372845	246827	88848.65	12007	18794	4609	988	210	277	182	65.2	19.9	13.8
66	16.37	0.41	0.0588	0.00127	0.01931	0.000483	1900	42200	518987	451876	314655	231072	82297.3	12575	16432	3449	833	164	212	144	8.9	17.4	0.0
67	16.36	0.40	0.0541	0.00114	0.01942	0.000473	2520	30760	554008	451876	355603	263020	112702.7	15293	23266	5789	1362	313	401	203	46.6	21.7	19.1
68	16.58	0.40	0.0536	0.00114	0.01947	0.000486	4360	30500	551055	445351	365302	253611	106891.9	12895	21859	5180	1167	253	342	175	54.3	10.6	2.8
69	16.48	0.36	0.0544	0.00126	0.01949	0.000443	2458	38700	540506	474715	376078	270460	98175.68	12860	19598	4571	1020	230	319	166	40.5	14.3	13.0
70	16.53	0.39	0.0532	0.00121	0.01933	0.00046	2109	32100	576371	450408	367457	266521	106081.1	13606	20251	4535	1053	232	317	178	28.3	21.7	0.0
71	16.44	0.44	0.0542	0.0013	0.01924	0.00052	1890	47000	562447	438825	335129	252079	98310.81	12877	19246	4321	959	221	321	186	34.0	13.7	19.1
72	16.48	0.42	0.0544	0.00118	0.01953	0.000499	1660	34700	583966	491028	385776	286433	96013.51	13819	19749	4488	1179	283	364	203	44.5	15.5	8.5
73	16.27	0.40	0.0557	0.00123	0.01927	0.000501	1970	86900	597046	405067	315733	243107	80135.14	11545	15829	3399	813	159	214	136	31.6	16.1	11.8
74	16.18	0.41	0.0540	0.00127	0.01937	0.000484	2270	37100	594937	442088	334052	248578	89054.05	12078	18492	3853	833	192	251	157	15.0	16.8	13.4
75	16.17	0.38	0.0535	0.00122	0.01985	0.000459	2460	31100	580591	451876	365302	266740	116216.2	14174	23317	5568	1276	276	394	232	25.5	26.1	14.6
76	16.11	0.38	0.0542	0.00126	0.01946	0.000452	1563	33400	582278	446982	348060	269147	104729.7	14121	20251	4479	984	219	271	175	22.3	9.3	8.9

Solid Earth Discussions — Open Access EGU

Table 3. U/Th–Pb analytical data for zircon (n= 83) from Sobrado paragneises sorted by 206Pb/238U age. 238U/206Pb and 207Pb/206Pb isotopic ratios are corrected for baselines, time-dependent laser-induced inter-element fractionation, plasma-induced fractionation, and instrument drift. Error corresponds to 2σ

Spot	Description	206Pb/238U Age	±	238U/206Pb	±	207Pb/206Pb	±
8	c (h)	0.0	0.0	-59665.87	-1510.22	0.5760	0.0115
36	c (h)	0.0	0.0	-123152.70	-5989.82	0.6165	0.0126
15	r	380.3	8.7	16.48	0.38	0.0532	0.0012
59	c (h)	387.9	9.2	16.11	0.39	0.0553	0.0011
25	r	396.9	9.8	15.77	0.40	0.0535	0.0011
76	r	409.6	10.9	15.27	0.41	0.0537	0.0012
79	r	421.9	13.8	14.77	0.49	0.0559	0.0013
20	r	432.7	16.4	14.41	0.56	0.0552	0.0012
17	c (s)	445.5	11.0	13.99	0.35	0.0552	0.0012
70	r	458.2	11.6	13.59	0.35	0.0555	0.0012
53	m	462.8	12.9	13.42	0.38	0.0570	0.0013
10	c (h)	468.1	12.5	13.28	0.36	0.0563	0.0012
29	m	473.6	23.2	12.97	0.64	0.0652	0.0050
71	r	482.8	12.0	12.87	0.33	0.0561	0.0012
26	c (s)	485.9	13.2	12.77	0.35	0.0569	0.0013
11	c (h)	486.3	12.0	12.76	0.32	0.0573	0.0012
7	c (b)	489.2	12.8	12.48	0.33	0.0691	0.0014
67	c (h)	492.8	11.2	12.58	0.29	0.0572	0.0012
75	c (o)	493.1	12.5	12.59	0.33	0.0561	0.0012
47	m	501.7	11.6	12.35	0.29	0.0578	0.0014
61	c (h)	502.4	12.3	12.35	0.31	0.0568	0.0012
63	c (h)	508.6	13.1	12.15	0.32	0.0593	0.0014
34	o	511.2	12.4	12.12	0.30	0.0572	0.0012
74	m	518.7	14.1	11.93	0.33	0.0578	0.0016
12	o	520.8	12.2	11.90	0.28	0.0565	0.0015
55	c (o)	522.5	12.9	11.83	0.30	0.0584	0.0013
6	c (o)	522.9	11.6	11.81	0.27	0.0596	0.0012
33	o	523.1	15.0	11.83	0.35	0.0576	0.0013
13	c (o)	526.7	12.3	11.75	0.28	0.0577	0.0013
42	c (o)	530.3	13.8	11.66	0.31	0.0586	0.0013
68	c (o)	530.4	13.8	11.66	0.31	0.0584	0.0015
57	c (o)	531.7	14.2	11.61	0.32	0.0591	0.0013
27	c (s)	531.9	15.1	11.63	0.34	0.0579	0.0015
62	c (o)	532.3	13.4	11.61	0.30	0.0583	0.0012
60	m	538.0	12.8	11.48	0.28	0.0588	0.0013
43	c (o)	543.2	15.2	11.36	0.33	0.0590	0.0013
52	c (o)	545.2	14.0	11.31	0.30	0.0597	0.0014
56	c (s)	548.9	14.9	11.27	0.31	0.0569	0.0017
64	c (o)	549.3	13.0	11.25	0.27	0.0581	0.0012
69	c (h)	553.6	13.4	11.19	0.28	0.0563	0.0015
14	c (h)	566.8	14.7	10.88	0.29	0.0590	0.0013
73	r	583.8	16.4	10.31	0.30	0.0771	0.0018

Spot	Description	206Pb/238U Age	±	238U/206Pb	±	207Pb/206Pb	±
19	o	589.2	14.6	10.45	0.27	0.0595	0.0013
77	m	657.1	19.4	9.05	0.27	0.0837	0.0017
78	r	660.8	18.2	9.03	0.25	0.0808	0.0018
30	r (o)	844.0	27.5	6.85	0.23	0.0992	0.0022
45	c (s)	884.1	26.3	6.52	0.20	0.0998	0.0022
41	c (h)	891.1	28.8	6.41	0.21	0.1071	0.0025
9	o	968.7	27.7	5.89	0.17	0.1056	0.0023
50	c (o)	1148.4	32.7	4.88	0.14	0.1147	0.0023
58	c (o)	1172.2	33.0	4.76	0.14	0.1165	0.0024
46	c (h)	1217.1	33.7	4.80	0.14	0.0823	0.0017
38	c (o)	1243.4	40.8	4.67	0.16	0.0874	0.0020
31	m	1312.2	39.2	4.23	0.13	0.1184	0.0026
22	c (h)	1881.0	37.5	3.76	0.09	0.1151	0.0024
24	c (h)	1910.0	37.8	3.84	0.13	0.1169	0.0025
65	c (s)	1955.8	36.0	3.71	0.09	0.1200	0.0024
81	c (o)	1959.9	37.7	4.07	0.11	0.1203	0.0025
23	c (o)	1972.5	38.6	4.10	0.14	0.1211	0.0026
54	m	1975.1	38.0	3.96	0.11	0.1213	0.0026
39	c (o)	1987.4	36.6	3.23	0.09	0.1221	0.0025
1	c (s)	1992.8	38.0	3.76	0.10	0.1225	0.0026
44	c (o)	2020.3	36.3	2.81	0.09	0.1244	0.0026
21	o	2028.4	35.8	3.40	0.08	0.1250	0.0025
16	c (o)	2032.3	36.5	3.40	0.08	0.1253	0.0026
5	m	2035.3	36.6	2.93	0.08	0.1255	0.0026
83	c (s)	2055.5	37.9	3.18	0.09	0.1269	0.0027
80	c (s)	2064.9	36.1	2.75	0.07	0.1276	0.0026
32	o	2080.3	36.5	3.00	0.08	0.1287	0.0027
40	m (s)	2095.5	36.4	2.79	0.08	0.1298	0.0027
48	c (s)	2099.3	38.1	2.99	0.12	0.1301	0.0028
4	c (h)	2102.5	35.4	3.17	0.08	0.1303	0.0026
37	c (s)	2106.6	35.8	2.79	0.06	0.1306	0.0027
51	c (o)	2110.5	35.4	3.37	0.09	0.1309	0.0026
18	c (o)	2184.0	36.8	3.12	0.08	0.1366	0.0029
35	o	2204.8	36.9	3.35	0.09	0.1382	0.0029
66	c (o)	2433.4	34.3	3.39	0.09	0.1579	0.0032
49	c (o)	2466.1	35.0	3.26	0.09	0.1610	0.0033
2	r	2541.6	33.8	2.82	0.07	0.1684	0.0034
28	c (h)	2584.9	35.0	2.99	0.08	0.1728	0.0036
72	r	2596.0	33.9	2.38	0.06	0.1740	0.0035
82	c (b)	2624.5	33.6	2.48	0.07	0.1770	0.0036
3	c (h)	2691.4	33.6	2.37	0.05	0.1842	0.0037

Table 4. Chondrite-normalized U, Th and REE (La, Ce, Pr, Nd, Sm, Eu, Gd, Tb, Dy, Ho, Er, Tm, Yb, Lu) expressed in ppm for zircons (n= 83) from Sobrado paragneises sorted by 206Pb/238U age. Grain description: c, core; r, rim; m, mantle; s, sectorial; h, homogeneous; b, soccerball. Th/U, Yb/Gd, Eu/Eu*, Ce/Sm, Lu/Dy, U/Ce isotopic ratios are included.

Spot	Descriptor	U (ppm)	Th (ppm)	Hf (ppm)	La (ppm)	Ce (ppm)	Pr (ppm)	Nd (ppm)	Sm (ppm)	Eu (ppm)	Gd (ppm)	Tb (ppm)	Dy (ppm)	Ho (ppm)	Er (ppm)	Tm (ppm)	Yb (ppm)	Lu (ppm)	Th/U	Yb/Gd	Eu/Eu*	Ce/Sm	Lu/Dy	U/Ce
8	c (h)	937	352	118738	0.13	29.04	3.49	9.41	45.27	22.38	337	609	1451	2381	3575	4818	5839	6870	0.38	29.63	0.18	2.66	0.47	53
36	c (h)	1837	213	191262	97.47	234.91	360.99	678.34	1304.05	710.48	980	590	691	934	1188	1866	2845	4106	0.12	0.61	0.63	0.75	0.59	13
15	r	224	30	113786	0.38	3.33	0.67	3.06	17.91	8.35	126	47	115	39	79	26	35	34	0.13	0.71	0.26	0.77	0.07	110
59	c (h)	989	54	115728	0.04	7.01	3.60	8.71	46.49	57.19	32	128	46	83	84	62	56	52	0.05	0.74	0.75	0.63	0.05	230
25	r	325	23	117864	0.04	2.64	0.48	1.38	11.35	7.99	40	36	46	60	84	155	213	309	0.07	4.06	0.42	0.96	0.67	200
76	r	223	27	121068	0.03	2.95	0.91	2.74	15.81	14.39	38	51	57	49	54	69	86	106	0.12	1.63	0.59	0.77	0.19	123
79	r	272	15	114466	0.05	0.86	0.68	1.88	7.84	6.04	43	142	277	330	292	231	177	170	0.06	2.89	0.34	0.46	0.06	514
20	r	258	17	118447	0.02	2.20	0.60	1.77	9.59	6.75	46	75	142	258	375	607	807	935	0.06	40.48	0.33	0.95	0.66	191
17	c (s)	337	12	126214	0.06	1.89	0.52	1.53	6.22	4.97	27	111	208	383	625	1263	1870	2439	0.03	29.29	0.29	1.26	1.17	291
70	r	378	7	126117	0.08	1.45	0.10	0.96	5.07	3.91	35	99	271	463	689	927	1093	1179	0.02	17.14	0.33	1.19	0.44	425
53	m	253	8	123981	0.09	1.22	0.18	0.59	4.19	3.55	66	122	235	372	541	644	652	626	0.03	13.00	0.29	1.21	0.27	338
10	c (h)	393	91	104563	0.03	57.59	0.64	2.12	9.05	6.75	32	72	283	504	813	1316	1764	2480	0.23	17.39	0.28	26.34	0.88	11
29	m	261	11	116505	0.05	3.13	0.27	0.81	3.38	3.20	35	136	179	295	488	785	1075	1488	0.04	40.00	0.31	3.84	0.83	136
71	m	301	7	123204	0.13	2.76	1.83	4.16	7.64	4.44	146	227	326	582	938	1433	1820	2276	0.02	27.14	0.27	1.50	0.70	178
26	c (s)	125	103	94660	0.05	21.86	2.38	5.86	41.08	29.66	143	211	393	625	901	1239	1553	1976	0.82	6.39	0.38	2.20	0.50	9
11	c (h)	601	358	131456	0.05	36.87	1.93	4.60	36.89	23.09	106	165	427	647	1019	1615	2373	3215	0.60	4.89	0.52	4.14	0.75	27
7	c (b)	763	40	131553	0.87	9.15	10.13	11.36	28.78	23.60	60	199	404	661	404	1822	2658	3374	0.05	9.80	0.08	1.32	0.83	136
67	c (h)	394	4	122330	0.05	0.46	0.50	1.86	7.50	1.60	48	157	313	348	369	340	314	350	0.01	15.00	0.52	0.25	0.11	1407
75	c (o)	222	5	119417	0.26	1.11	1.01	1.77	7.09	4.44	43	124	299	366	412	413	360	423	0.02	7.65	0.24	0.65	0.14	326
47	m	173	2	120291	0.05	0.17	0.05	0.42	5.20	3.02	46	106	247	229	193	186	182	199	0.01	8.67	0.20	0.14	0.08	1619
61	c (h)	166	25	100291	0.05	12.07	0.44	1.31	10.07	7.46	553	861	241	366	534	806	1118	1398	0.15	5.52	0.35	4.97	0.58	22
63	c (h)	122	804	22524	0.74	64.11	20.58	62.36	185.81	467.14	116	553	1191	1363	1688	2126	2193	2309	6.59	1.11	1.46	1.43	0.19	3
34	o	296	229	109515	0.06	112.07	0.56	2.19	18.51	10.48	56	249	524	1007	1506	2324	2969	3943	0.77	24.81	0.23	25.07	0.75	4
74	m	48	38	92427	0.08	14.71	1.48	1.53	7.57	16.16	75	121	267	445	749	1255	1503	2114	0.78	9.09	0.79	8.05	0.79	5
12	o	74	55	84175	0.05	19.90	0.60	3.63	20.34	11.90	67	112	241	443	608	915	1286	1537	0.75	7.50	0.30	4.05	0.64	6
55	c (o)	215	71	99515	0.04	16.66	0.60	14.73	14.73	10.83	799	335	303	496	875	1215	1553	2130	0.33	12.92	0.34	4.68	0.70	21
6	c (o)	1215	931	83883	0.33	85.32	22.41	175.05	175.00	78.51	234	1127	2130	3205	4256	5980	7205	8699	0.77	12.47	0.21	2.02	0.41	23
33	o	82	69	77184	0.13	57.10	2.70	34.14	53.31	79.40	72	335	715	1081	1769	2725	3534	4634	0.84	7.16	0.71	4.44	0.65	2
13	c (o)	184	64	96602	0.01	14.68	0.51	10.09	44.26	8.88	157	97	262	467	719	1053	1360	1923	0.35	10.56	0.31	5.49	0.73	20
42	c (o)	136	114	70291	0.15	26.59	3.59	14.22	8.65	58.97	39	615	382	641	950	1547	2000	2642	0.84	6.67	0.71	2.49	0.69	8
68	c (o)	66	47	93981	0.07	23.00	0.38	2.41	97.30	11.55	360	103	172	262	478	652	842	1224	0.71	4.69	0.63	11.02	0.71	5
57	c (o)	119	117	74175	0.11	33.77	4.64	21.88	10.47	22.02	71	202	1085	1676	2350	2862	3385	3817	0.99	23.91	0.12	1.44	0.35	6
27	c (s)	61	45	90097	0.01	21.40	0.59	2.67	38.45	8.70	108	248	213	352	523	814	1056	1411	0.74	6.25	0.32	8.46	0.66	5
62	c (o)	456	176	98058	0.05	21.70	2.33	7.26	50.68	30.02	130	152	365	588	962	1421	2087	2907	0.39	4.62	0.47	2.34	0.80	34
60	m	148	95	93107	0.12	31.32	4.38	13.37	22.77	41.03	77	217	442	617	906	1360	1646	2150	0.64	6.22	0.51	2.56	0.49	8
43	c (o)	119	68	84466	0.05	11.00	0.75	3.94	15.68	27.18	95	402	326	496	773	1202	1559	2053	0.57	6.25	0.65	2.00	0.63	18
52	c (o)	113	49	110874	0.02	36.87	0.55	2.10	49.66	16.16	242	224	480	830	1400	2117	2944	4024	0.44	9.09	0.42	9.74	0.84	5
56	c (s)	37	66	90971	0.09	118.60	1.95	7.07	20.27	27.53	101	121	793	1201	1756	2275	2522	3256	1.77	13.41	0.25	9.89	0.41	1
64	c (o)	409	196	122136	0.05	45.35	0.86	3.41	20.27	1.78	57	116	480	835	1513	2275	2783	3638	0.48	30.00	0.04	9.27	0.76	15
69	c (h)	39	33	100583	0.01	19.90	0.66	1.82	12.16	14.03	72	189	226	374	623	834	1118	1553	0.84	5.25	0.53	6.78	0.69	3
14	c (h)	264	120	108835	0.01	27.08	1.31	2.47	11.35	3.91	72	116	253	449	688	1113	1404	1955	0.45	13.85	0.14	9.88	0.77	16
73	r	238	34	114369	0.09	10.28	1.86	4.97	21.62	15.81	75	189	289	447	575	810	901	1150	0.14	6.36	0.39	1.97	0.40	38

Table 4 (Cont.)

Spot	Description	U (ppm)	Th (ppm)	Hf (ppm)	La (ppm)	Ce (ppm)	Pr (ppm)	Nd (ppm)	Sm (ppm)	Eu (ppm)	Gd (ppm)	Tb (ppm)	Dy (ppm)	Ho (ppm)	Er (ppm)	Tm (ppm)	Yb (ppm)	Lu (ppm)	Th/U	Yb/Gd	Eu/Eu*	Ce/Sm	Lu/Dy	U/Ce
19	o	224	185	100388	0.02	38.34	1.07	3.89	27.91	9.77	136	252	569	1004	1563	2413	3019	3813	0.83	34.50	0.16	5.69	0.67	10
77	m	397	18	123301	0.38	3.07	1.47	3.00	19.12	12.43	74	158	205	203	248	331	400	423	0.05	2.48	0.33	0.66	0.21	211
78	r	157	40	85631	0.18	11.75	1.50	1.95	6.01	11.19	28	53	89	121	238	416	573	907	0.26	3.62	0.86	8.09	1.02	22
30	r(o)	270	29	111068	0.04	4.26	0.24	0.94	6.15	6.22	55	120	256	410	628	955	1137	1402	0.11	13.53	0.34	2.87	0.55	103
45	c(s)	65	29	100971	0.05	7.94	0.17	1.05	9.32	8.35	26	66	132	194	333	474	609	793	0.45	6.19	0.54	3.53	0.60	13
41	c(h)	36	16	94660	0.03	15.01	0.44	1.55	7.09	9.77	47	71	138	225	406	619	814	1061	0.45	8.64	0.53	8.76	0.77	4
9	o	53	45	82718	0.03	35.73	1.76	4.99	21.35	13.68	101	129	269	434	559	789	1106	1358	0.84	7.62	0.30	6.93	0.50	2
50	c(o)	321	114	97087	0.38	18.76	0.80	3.74	14.46	18.29	59	108	226	379	621	976	1205	1565	0.35	8.21	0.62	5.37	0.69	28
58	c(o)	463	39	113010	0.30	4.32	1.37	2.47	15.54	14.92	59	124	200	273	375	502	632	850	0.08	2.94	0.49	1.15	0.43	175
46	c(h)	275	126	105825	0.03	41.60	0.69	3.44	25.34	3.37	137	260	488	766	1288	1753	2112	2817	0.46	23.13	0.06	6.80	0.58	11
38	c(o)	48	27	84078	0.05	13.51	1.23	4.46	22.50	9.59	107	174	341	549	869	1150	1547	2033	0.56	10.87	0.20	2.49	0.60	6
31	m	41	17	95728	0.04	15.50	0.22	0.83	6.08	4.97	13	29	51	104	181	307	492	720	0.41	6.40	0.57	10.56	1.40	4
22	c(h)	128	32	117573	0.01	1.75	0.68	2.52	9.59	1.15	26	23	54	61	102	136	167	199	0.25	8.14	0.07	0.75	0.37	119
24	c(s)	166	71	124078	0.02	6.04	1.00	3.04	17.91	4.97	86	94	126	132	143	153	151	157	0.43	2.56	0.13	1.40	0.12	45
65	c(o)	407	6	79709	0.02	0.44	0.29	0.88	13.58	2.13	89	216	261	218	1025	213	239	239	0.02	3.55	0.06	0.13	0.09	1508
81	c(o)	80	47	90291	0.08	24.96	0.89	2.54	12.97	32.68	65	158	296	542	1025	1615	2348	3687	0.59	5.96	1.12	7.97	1.25	5
23	m	71	51	97379	0.03	28.71	1.33	3.92	19.26	15.45	84	120	221	368	566	818	1236	1602	0.71	6.92	0.38	6.18	0.72	4
54	c(o)	66	43	92039	0.31	22.51	0.82	3.79	16.28	10.48	76	125	205	344	533	794	981	1329	0.64	5.45	0.30	5.73	0.65	5
39	c(s)	125	113	89126	0.08	61.34	0.46	4.16	15.95	18.83	75	134	259	408	631	866	1261	1565	0.90	6.67	0.54	15.93	0.60	3
1	c(s)	52	36	83786	22.83	74.39	75.75	54.05	50.00	16.87	84	97	213	346	534	798	1186	1602	0.70	6.25	0.26	6.16	0.75	1
44	o	100	109	110194	0.17	44.05	1.35	6.46	32.43	27.18	125	182	351	526	813	1097	1385	1772	1.09	5.43	0.43	5.63	0.50	1
21	o	587	251	98835	0.04	20.39	0.71	1.88	9.59	5.51	54	96	198	379	609	1000	1311	1748	0.43	10.40	0.24	8.80	0.88	47
16	m	118	107	99767	8.02	83.20	86.21	78.77	76.35	27.89	118	124	251	425	650	1016	1478	2028	0.91	4.09	0.29	4.51	0.81	2
5	c(s)	70	102	81942	0.01	25.61	0.58	1.33	5.81	4.80	36	60	136	222	373	595	786	1183	1.47	9.33	0.33	18.26	0.87	4
83	c(s)	48	22	98738	0.02	8.65	0.32	0.77	4.80	5.15	14	28	41	86	168	232	370	549	0.47	4.41	0.62	7.46	1.32	9
80	o	46	34	103010	0.04	30.67	0.41	1.47	9.66	8.70	46	85	150	256	424	725	888	1240	0.74	7.08	0.41	13.15	0.83	2
32	m(s)	101	49	89709	0.27	49.92	0.69	3.15	10.07	7.28	36	71	123	229	406	704	1025	1488	0.49	13.75	0.38	20.54	1.21	3
40	c(s)	62	40	91553	0.02	34.26	0.56	2.04	12.84	13.85	64	94	185	302	483	704	395	1329	0.64	3.87	0.48	11.05	0.72	3
48	c(h)	28	15	110194	0.03	13.88	0.53	1.09	3.45	6.04	21	35	74	100	194	285	66	630	0.53	3.15	0.72	16.69	0.86	3
4	c(s)	677	299	94951	0.01	21.04	0.66	1.40	9.59	4.80	72	140	327	579	1025	1595	2329	3443	0.44	32.31	0.18	9.08	1.05	52
37	c(s)	151	53	107767	0.21	22.02	0.64	1.68	13.85	6.22	87	170	343	661	1150	1947	2391	3610	0.35	13.85	0.18	6.59	1.05	11
51	c(o)	304	97	91553	0.05	6.82	0.72	2.76	16.96	3.91	71	145	273	480	800	1089	1509	2167	0.32	17.65	0.11	1.67	0.79	73
18	o	49	19	99515	0.08	10.77	0.73	1.01	9.12	5.51	42	80	186	344	500	846	1081	1439	0.38	17.33	0.28	4.89	0.77	7
35	o	182	124	106699	0.23	3.38	0.53	2.54	13.31	4.09	68	98	170	260	328	478	522	679	0.68	10.00	0.14	1.05	0.40	88
66	c(o)	693	223	125922	0.11	16.97	1.29	4.75	17.16	44.23	59	116	204	352	580	781	1081	1411	0.32	2.17	1.39	4.09	0.69	67
49	c(o)	403	115	105728	0.09	2.28	0.54	2.01	20.07	1.74	93	161	232	251	306	348	337	386	0.29	11.58	0.04	0.47	0.17	288
2	r	444	141	98350	0.48	8.40	1.38	2.54	15.68	7.82	90	129	267	425	611	899	1118	1610	0.32	8.18	0.21	2.22	0.60	86
28	c(h)	878	74	110194	0.03	11.97	4.04	6.48	16.82	8.88	35	61	97	171	259	445	646	878	0.08	7.78	0.37	2.95	0.90	120
72	r	495	22	129029	0.07	7.26	0.39	0.61	4.73	3.37	34	65	145	229	432	700	994	1504	0.04	16.92	0.27	6.36	1.04	111
82	c(b)	280	136	96505	0.07	3.34	0.82	3.22	22.16	2.49	76	151	215	242	269	308	269	250	0.48	9.17	0.06	0.63	0.12	137
3	c(h)	690	223		0.10	12.72	2.78	7.72	48.58	15.28	233	280	577	837	1231	1846	2304	2959	0.32	10.91	0.14	1.08	0.51	88